

UNCLASSIFIED



Australian Government
Department of Defence
Defence Science and
Technology Organisation

Radon Spectrum and Its Application for Small Moving Target Detection

Yunhan Dong

National Security and ISR Division
Defence Science and Technology Organisation

DSTO-TR-3103

ABSTRACT

Analogous to the radar Doppler spectrum for coherent processing, the concept of a Radon spectrum that is a kind of normalised Radon transform is proposed and used for radar non-coherent detection. One advantage of using the Radon transform for non-coherent processing is that integration in all directions is considered, and hence range migration of moving targets is not a concern. The detection processing is based upon a 2D Radon spectrum that is transformed from the original range-time 2D radar image. The threshold and the probability of detection for a given false-alarm rate are determined in the same way as the traditional non-coherent integration. Both simulated and real radar datasets are tested and the effectiveness of the proposed technique is demonstrated.

RELEASE LIMITATION

Approved for public release

UNCLASSIFIED

UNCLASSIFIED

Published by

*National Security and ISR Division
DSTO Defence Science and Technology Organisation
PO Box 1500
Edinburgh South Australia 5111 Australia*

*Telephone: 1300 DEFENCE (1300 333 363)
Fax: (08) 7389 6567*

*© Commonwealth of Australia 2015
AR-016-290
April 2015*

APPROVED FOR PUBLIC RELEASE

UNCLASSIFIED

UNCLASSIFIED

Radon Spectrum and Its Application for Small Moving Target Detection

Executive Summary

In support of the AIR 7000 project and with the goal to improve the performance of the APY-10 radar being acquired with P-8A Poseidon maritime patrol aircraft, the author proposed in this report a radar detection technique for small moving target detection in non-coherent processing, possibly applicable to the detection mode for small moving targets.

To detect a small radar target from a radar noisy environment, such as the sea surface, the common practice includes increasing range resolution to reduce the intake of sea clutter and hence increase signal-to-clutter ratio (SCR) for range bins, as well as increasing the time interval of data collection (for instance, using a scan-to-scan process) to decorrelate sea clutter and reduce the influence of sea spikes. By doing these, however, the so-called range bin migration often occurs if the target of interest is not stationary, making the traditional non-coherent integration problematic.

If the motion of a moving target is rectilinear during the period of data collection, its trace in the range-time 2D imagery is a linear pattern whose detection is best performed by the Radon or Hough transform.

Analogous to the radar Doppler spectrum for coherent processing, the concept of a Radon spectrum, which is a kind of normalised Radon transform, is introduced for non-coherent processing. The detection processing is based upon the 2D Radon spectrum that is transformed from the original range-time 2D radar image, similar to the detection based on range-Doppler spectrum after the Fourier transform for coherent processing. The threshold and the probability of detection for a given false-alarm rate are determined accordingly in the same way as the traditional non-coherent processing.

Whether there is range migration of a moving target is not a concern and it does not make any difference to the detection with the use of the Radon spectrum, provided the movement of the target is rectilinear. A stationary target is only a special case of zero velocity and the associated result given by the Radon spectrum shall be identical to the traditional non-coherent integration. Continuous exposure of the target to the radar is not required during the data collection, as long as its trace is rectilinear and the trace is captured by the radar.

UNCLASSIFIED

UNCLASSIFIED

Both simulated and real radar datasets have been tested and demonstrate the effectiveness of the proposed detection mode. It has been shown that a moving target with a few dB SCR can be detected robustly from a very spiky and highly correlated sea clutter situation at a given false-alarm rate of 10^{-6} .

UNCLASSIFIED

UNCLASSIFIED

Author

Yunhan Dong

National Security and ISR Division

Dr Yunhan Dong received his Bachelor and Master degrees in 1980s in China and PhD in 1995 at UNSW, Australia, all in electrical engineering. He then worked at UNSW from 1995 to 2000, and Optus Telecommunications Inc from 2000 to 2002. He joined DSTO as a Senior Research Scientist in 2002. His research interests are primarily in radar signal and image processing and clutter analysis. Dr Dong was a recipient of both the Postdoctoral Research Fellowships and Research Fellowships from the Australian Research Council.

UNCLASSIFIED

UNCLASSIFIED

This page is intentionally blank

UNCLASSIFIED

Contents

1. INTRODUCTION.....	1
2. CLUTTER AND TARGET MODELS.....	3
3. CHOICE OF AMPLITUDE, INTENSITY OR DATA IN DECIBELS.....	8
4. RADON TRANSFORM AND RADON SPECTRUM	12
4.1 Radon Transform.....	12
4.2 Radon Spectrum.....	14
5. EXAMPLES.....	18
5.1 A Simulated Case.....	19
5.2 Christmas Island S-band Data.....	23
5.3 X-band Data	29
5.3.1 Sea Clutter Only Dataset	30
5.3.2 Sea Clutter with Target Dataset.....	35
5.4 Case of Airborne Ingara Data.....	38
6. CONCLUSIONS.....	47
7. ACKNOWLEDGEMENT.....	48
8. REFERENCES	49

Acronyms

1D	one-dimensional
2D	two-dimensional
cdf	cumulative distribution function
DC	direct current
DSTO	Defence Science and Technology Organisation
GPS	Global Positioning System
iid	independent and identically distributed
IMU	Inertial Measurement Unit
INU	Inertial Navigation Unit
pdf	probability density function
PRF	pulse repetition frequency
RCS	radar cross-section
RPM	revolutions per minute
SAR	synthetic aperture radar
SCR	signal-to-clutter ratio
SNR	signal-to-noise ratio

1. Introduction

Detecting small moving targets from a noisy radar environment, such as the sea surface, using microwave radar is often not an easy task because of the target's low radar cross-section (RCS) and strong reflections from the sea surface. Typical practices include using a finer radar range resolution to reduce the intake of sea clutter in each range cell and hence increase the signal-to-clutter ratio (SCR). Increasing the dwell time for coherent integration may help by improving the Doppler resolution (distributing clutter signal over more bins and/or separating a target from background clutter Doppler spread). For the scenario of a slowly moving target on the sea surface, the benefit of coherent integration may be limited as the velocity of the target may be comparable to the movement of sea swells and currents, and often sea swells produce large radar returns. In situations where the clutter is uncorrelated between successive looks and the target is stationary, then it is beneficial to employ scan-to-scan non-coherent integration to improve the target SCR. A number of radar techniques are well known to facilitate the de-correlation of sea clutter returns but the gain is limited by the requirement for a stationary target.

For radar systems with 10 metre range resolution cells, a 10 knot radial speed point target will take less than 2 seconds to cross the cell, even with a high update radar system operating at 300 scans per minute. This would limit the integration to less about 9 scans or potentially 4.8 dB of gain¹. Many small target detection radar systems employ range resolution cells as small as 0.3 metre (reducing clutter power by 15 dB relative to the 10 metre cell), in which case a point target would have moved from the cell before the next scan. The situation is significantly better for range extended targets but the general thrust remains, that compensation for range walk is required if significant gain is to be obtained from non-coherent scan-to-scan integration.

Detection of a moving target traversing range bins has been studied. In general the detection methods can be divided into two categories. In the first category, the movement of the target is estimated, and the shift in range bins compensated (to be shifted back). Typical methods in this category include the keystone formatting method (Perry et al. 1999; 2007)². This technique rescales the slow time as a function of the chirp waveform frequency, and uses one-dimensional interpolation over the deramped phase history of data to remove the linear range migration, so that a moving target will be residing in the same range bin after the keystone reformatting and pulse compression. Elimination of phase error caused by the acceleration of the moving target is also discussed in the literature. However, this technique generally requires a high signal-to-noise ratio (SNR) or SCR, so that the phase shift caused by the movement of target can be identified and rectified.

¹ The gain of non-coherent processing gain can vary from \sqrt{N} to N , and the value of \sqrt{N} is used in this report as a general and conservative indication. Detailed discussions can be found in Richards, M. A. (2013), "Non-coherent integration gain, and its approximation", Technical Memorandum (revised May 6 2013) in Richards, M. A. (2014), *Fundamentals of Radar Signal Processing*, (2nd edition), McGraw-Hill, New York.

² The technique was applied to the synthetic aperture radar (SAR) mode, not the real aperture mode discussed in the report, though.

Shaw (2013) in a stationary radar system used for coastal surveillance employed multiple parallel detection schemes identified as slow, moving, fast and raw. The moving detection scheme is a scan to scan integration with radial motion compensation implemented as a moving average of the motion compensated radar log video signal (see Section 3 for commentary on the use of the log video signal). The motion compensation covered 21 motion models with range walk steps of 0.1 range bins per scan to cover ± 1 range bin of walk per scan. The 21 motion compensated signals were then collapsed for detection purposes into the largest magnitude return for each post integration range bin over the 21 models, with the tracker being supplied the detection response and the identification of the motion model that was the source of the detected signal. Targets having speeds outside of the motion range of the moving models are addressed by other detection schemes.

Methods in the second category perform integration along different range bins which the moving target traverses during the integration time. In an earlier paper, Allen *et al.* (1989) proposed a simple geometric integration method to integrate target energy from the range bins that the target traversed. In this method, the range profile for the current pulse is re-sampled (interpolated), and the peak of the target response and its location are identified. Range profiles for successive pulses are processed in the same way. With the finding of the locations of the peak of the corresponding target, a proper integral path is established and the integration along that path is performed. More systematic ways to perform integration along different tilting paths is completed by the Hough transform and/or Radon transform (Carlson et al. 1994a; b; c; Xu et al. 2011; Yu et al. 2012). In the papers by Carlson et al. (1994a, b, and c), the Hough transform is used to detect target tracks, typically in a two-dimensional domain, such as in 2D range-time (here the time may refer to pulse/scan) imagery. Target traces in line patterns can also be detected using the Radon transform. Normally both the Hough and Radon transforms are only applicable to non-coherent integration. However, in the papers of Xu et al. (2011) and Yu et al. (2012), the Radon transform is further incorporated with the Fourier transform, so that the integration can be performed along a tilting line (via the Radon transform) and in a coherent manner (via the Fourier transform).

Based on the target of interest, this report investigates a detection technique using the Radon transform. The Radon transform is perhaps most powerful and useful in detecting line patterns, among other feature detections. Other transforms, such as the Hough transform are also commonly used in line extractions (Ballard 1981; Rosenberg 2012). However, the Radon transform and the Hough transform are equivalent to one another at least for a line detection, though the Hough transform is more popularly used to process binary images (Furukawa and Shinagawa 2003; Carlson et al. 1994c). In the report, the concept of a Radon spectrum is introduced based on the Radon transform. After introducing the concept of Radon spectrum, the detection threshold and probability of detection required by a given constant false-alarm rate (CFAR) can be determined in the same way as is used in the traditional non-coherent integration detection process. The difference between the traditional non-coherent integration and the proposed technique is that the former requires the target to reside in the same range bin during the integration time, while there is no such limitation for the latter. We will show shortly that if the range migration is linear, the integrated energy shown in the Radon spectrum will be exactly

equal to the energy of the non-coherent integration over the same but stationary or quasi-stationary target.

In principle we should consider both the motion in range and the motion in azimuth. However for the target set of interest to the current programme, the target speeds are low and the range of interest is relatively large. For a 1 degree, 3 dB beamwidth radar system, at 50 km the cross range covered by a beam is 0.87 km, which would require a speed of 28 knots to cross in one minute. The targets of interest have speeds less than 10 knots. The radar class under consideration has a scan rate of 300 revolutions per minute (RPM), and integrating over 300 scans there is potentially 12.4 dB of noise limited processing gain (correlation in background clutter will generally reduce the potential gain, see Section 5 for more details)³. For a stationary radar system, a 28 knot target would move over the full 3 dB beamwidth resulting in a 0.9 dB loss relative to an “on bore sight” target, whereas a 10 knot target would have a mean loss associated with neglecting azimuth crossing of 0.5 dB relative to the bore sight target⁴. For a moving radar system, the situation is more complex due to the need to spatially register successive radar scans, however for the purposes of this study, we will assume that the registration is effectively perfect (a case where this fails is examined in Subsection 5.4) allowing us to neglect crossing motion for the ranges and targets speeds of interest with only a small loss in potential processing gain.

This report is organised in the following way: clutter and target models are reviewed in Section 2; what data quantities should be used in the non-coherent integration processing are discussed in Section 3; the Radon transform and the Radon spectrum are presented in Section 4; case studies using both simulated data and real radar data are presented in Section 5 and finally conclusions are given in Section 6.

2. Clutter and Target Models

We assume sea clutter to be K-distributed as this distribution has been widely observed (Ward et al. 2006; Crisp et al. 2006). The target signal is assumed to vary with the Swerling I model, i.e., its in-phase and quadrature signals each vary from scan-to-scan in a Gaussian fashion. The distribution of the clutter plus the target signal has, unfortunately, no closed-form expression. Watts (1987) has studied the distribution of the combined K-distributed clutter plus Gaussian signal. He has approximated the combined distribution as a new K-distribution, with a modified shape parameter and a modified mean by equating the first and second moments of the approximated and the exact distributions. For K-distributed clutter with parameters of (μ_0, ν_0) (where μ_0 and ν_0 are the mean intensity and shape parameter, respectively), embedded with a complex Gaussian signal $CN(0, \sigma^2)$, the combination is approximated to a new K-distribution with parameters of (μ, ν) , where,

³ Also see Footnote 1.

⁴ The loss is an average loss so as to accommodate slower targets at both edges and the centre of the beam. The impact of the greater loss then depends critically on the beam overlap arrangements, and some high RPM systems have poor overlap – thanks to A. P. Shaw’s comment and input.

$$\mu = \mu_0 + \sigma^2 = \mu_0(1 + \beta) \quad (1)$$

$$\nu = \nu_0(1 + \beta)^2 \quad (2)$$

where $\beta = \sigma^2 / \mu_0$ is the signal-to-clutter ratio (SCR) of the target.

The approximated pdf/cdf (probability density function / cumulative distribution function) starts separating from the exact distribution only at the very end of the upper tail, normally in the $P_{fa} = 10^{-6}$ or smaller region (Dong 2012b). Therefore, the approximation is sufficiently accurate for normal radar detection studies. The pdf of the K-distribution is given by,

$$p(z) = \frac{2b}{\Gamma(\nu)} (bz)^{(\nu-1)/2} K_{\nu-1}(2\sqrt{bz}) \quad 0 \leq z \leq \infty \quad (3)$$

Where $z = |x|^2$ denotes the intensity of K-distributed data (x is the baseband complex I/Q data), $b = \nu / \mu$, $\Gamma(\cdot)$ is the Gamma function and $K_\nu(\cdot)$ is the modified Bessel function of the second kind.

The pdf of the amplitude of the K-distributed data is given by,

$$p(t) = \frac{2q}{\Gamma(\nu)} \left(\frac{qt}{2} \right)^\nu K_{\nu-1}(qt) \quad 0 \leq t \leq \infty \quad (4)$$

where $t = |x|$ and q is a scale parameter, given by,

$$q = 2\sqrt{\nu / \mu} = 2\sqrt{b} \quad (5)$$

Noting $dz/dt = 2t$, one finds (3) and (4) to be identical.

Note that the K-distribution of sea clutter is often said to be a compound K-distribution consisting of a slowly-varying Gamma component and a fast-varying Gaussian component (Ward et al. 2006). The slowly-varying component may be considered as a constant (fully correlated) and the fast-varying component is partially or fully uncorrelated for pulse-to-pulse processing. However, for scan-to-scan processing, both the fast-varying and slowly-varying components may be considered as fully uncorrelated. Therefore, for scan-to-scan radar data, there is generally no need to treat the fast-varying and slowly-varying components separately. In fact, the separation of the two is usually not feasible.

To analyse the detection performance of a target detector, we need to know the distribution of the multi-look processed data with and without target signals. For the K-distribution, unfortunately, even with the assumption of all samples being independent and identically distributed (iid), the distribution does not in general have a closed-form irrespective of whether the multi-look processing uses intensity, amplitude or data in decibels (i.e. $10\log_{10} z$ or $20\log_{10} t$). Having said this, however, for K-distributed amplitude data with special shape values of $\nu = 0.5$, $\nu = 1.5$ and $\nu = m + \frac{3}{2}$, $m = 1, 2, \dots$, closed-form expressions have been found (Armstrong and Griffiths 1991).

For $\nu = 0.5$, $K_\nu(\cdot)$ reduces to,

$$K_{\pm 0.5}(t) = \sqrt{\frac{\pi}{2z}} e^{-t} \quad (6)$$

Equation (4) simplifies to,

$$p(t) = q \exp(-qt) \quad (7)$$

The pdf of a Gamma distribution is given by,

$$p_1(t) = \frac{q^a}{\Gamma(a)} t^{a-1} \exp(-qt) \quad (8)$$

where a is the shape parameter of the Gamma distribution (that differs from the shape parameter of the K-distribution). It can be seen that (7) is the case of Gamma distribution with $a = 1$.

It is well known that the distribution of the sum/mean of N independent Gamma distributed samples with a shape parameter a is still Gamma-distributed but with a shape parameter Na (Wilks 1962). Therefore, one can write the pdf of the mean of N K-distributed samples (when the quantity of amplitude is used in the averaging processing) with a shape parameter $\nu = 0.5$, as,

$$p_N(t) = \frac{qN}{\Gamma(N)} (qNt)^{N-1} \exp(-qNt) \quad (9)$$

where $t = \frac{1}{N} \sum_{i=1}^N t_i$

For $\nu = 1.5$, (4) reduces to,

$$p_1(t) = q^2 t \exp(-qt) \quad (10)$$

which is a case of the Gamma distribution with the shape parameter $a = 2$. Therefore the pdf of the mean of N such samples is,

$$p_N(t) = \frac{qN}{\Gamma(2N)} (qNt)^{2N-1} \exp(-qNt) \quad (11)$$

For $v = m + \frac{3}{2}$, $m = 1, 2, \dots$, the pdf of the mean of the N samples is given by (Armstrong and Griffiths 1991),

$$p_N(t) = qN \gamma^N \exp(-qNt) \sum_{j_0=0}^N \sum_{j_1=0}^{j_0} \sum_{j_2=0}^{j_1} \dots \sum_{j_{m-1}=0}^{j_{m-2}} \binom{N}{j_0} \binom{j_0}{j_1} \binom{j_1}{j_2} \dots \binom{j_{m-2}}{j_{m-1}} \times \frac{\beta_m^{N-j_0} \beta_{m-1}^{j_0-j_1} \dots \beta_0^{j_{m-1}}}{\Gamma(2N + j_0 + j_1 + \dots + j_{m-1})} (qNt)^{2N-1+j_0+j_1+\dots+j_{m-1}} \quad (12)$$

where

$$\gamma = \frac{\sqrt{\pi}}{2^{m+1} \Gamma(v)} \quad (13)$$

$$\beta_i = \frac{(m+i)!(m+1-i)}{2^i i!} \quad (14)$$

To verify the correctness of (12), a simulated dataset was generated. A dataset of 20×10^7 uncorrelated samples were generated, obeying the K distribution with a shape parameter $v = 3.5 = 2 + 3/2$, and a mean of $\mu = 1.0$. The dataset was multi-look processed to 10^7 samples and each was the mean amplitude of the original 20 samples ($N = 20$). The pdf of the simulated data and its theoretical pdf are shown in Figure 1, and the agreement between the two confirms the correctness of (12).

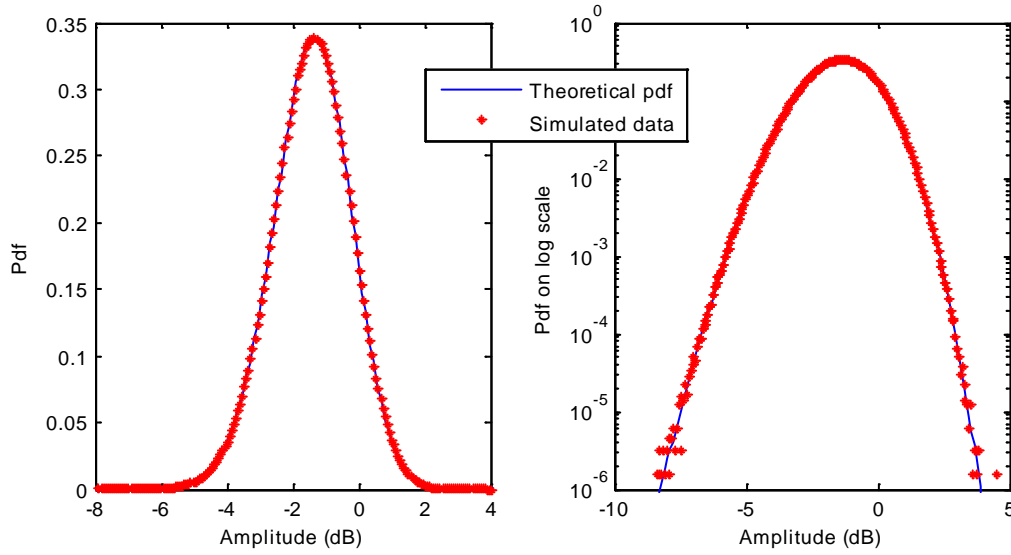


Figure 1: Comparison of the empirical pdf calculated from the simulated data and the theoretical pdf given by (12) (parameters used were: $N = 20$, $\nu = 2 + 3/2$ and $\mu = 1.0$).

Therefore, apart from a limited number of cases, the pdf of the multi-look K-distribution does not have a closed-form expression. In addition, even for the cases given by (9), (11) and (12), for a large N (for instance $N \geq 172$), the numerical calculation of the pdf in Matlab becomes problematic, as the largest number in the double format in Matlab is 1.7977×10^{308} , and $\Gamma(172) > 1.7977 \times 10^{308}$, so the calculation overflows/underflows⁵.

On the other hand, as shown in Figure 1, numerical simulation provides accurate pdf values once the number of samples are sufficiently large. It has been shown that for a desired probability P (be it either the false-alarm rate or probability of detection), to ensure an absolute relative error less than 5% for 95% of time, the number of iid samples used for numerical calculation is (Dong 2012a; Kay 1998, Chapter 2),

$$N_{total} = 1.59 \times 10^3 P^{-1} \quad (15)$$

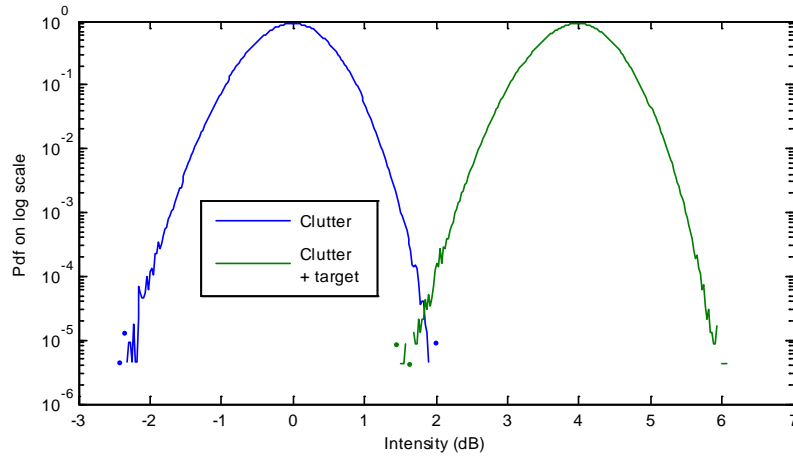
According to (15), for instance, to determine the threshold for $P_{fa} = 10^{-6}$, a total 1.59×10^9 samples shall ensure the absolute relative error of the calculated threshold to be less than 5% for 95% of time, irrespective of the distribution of the data. For calculating the probability of detection, the required number of samples is much smaller, as the range of interest of P_d often lies in $0.1 \leq P_d \leq 1$.

⁵ Such calculations in Mathematica do not seem to be a problem.

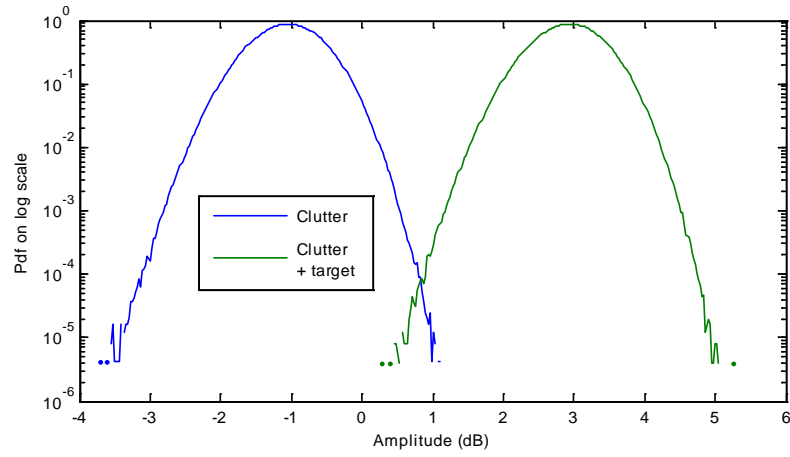
3. Choice of Amplitude, Intensity or Data in Decibels

In an earlier report (Dong 2012b), we have shown that an optimal detector should use the quantity of intensity for detecting Swerling II targets (target signal varies from pulse to pulse in a Gaussian fashion) embedded in the K-distributed clutter, regardless of the shape parameter, in the pulse-to-pulse non-coherent integration processing. This is because the slowly-varying component of the K-distributed is considered to be fully correlated (remain unchanged) from pulse to pulse, and hence the data undergo a local random Gaussian process rather than a global random K process. The question here is what quantity of data we should use in scan-to-scan non-coherent detection processing.

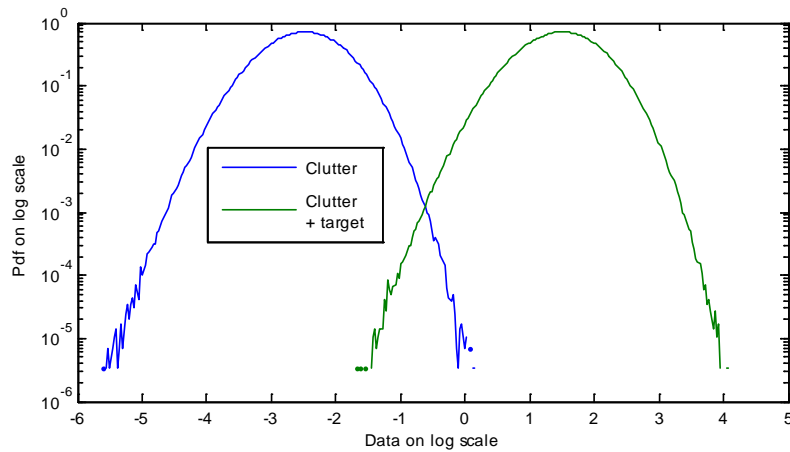
If the K-distributed clutter has a large shape parameter, its distribution approaches Gaussian. In such a case, for detecting Swerling I targets, one should use the intensity in the non-coherent integration, as such a detector is optimal. However, if the K-distributed clutter has a small shape parameter, the use of intensity may not be appropriate. The optimal detector in closed-form cannot be derived in general. Intuitively, one could imagine that the intensity, compared to other quantities such as amplitude and data in decibels (i.e. $10\log_{10} z$ or $20\log_{10} t$), overweights sea spikes (high returns) in the averaging processing resulting in a higher threshold (for the same false-alarm rate) and hence reduces the probability of detection. In other words, using the amplitude data or log data in the non-coherent integration will result in better detections for clutter with small shape parameters. To demonstrate, the empirical (numerically calculated) pdfs of clutter and clutter plus target after non-coherent integration using different quantities are shown in Figure 2, Figure 3 and Figure 4 for three different shape values, respectively. Each figure compares these pdfs for the same clutter and target parameters but using different quantities in the non-coherent integration. Since these pdfs are for the data after the non-coherent integration, the usual false-alarm rate of 10^{-6} for the original data becomes 10^{-4} for multi-look number of $N = 100$. It can be seen in the first case of $\nu = \infty$ shown in Figure 2 that the intensity data results in the best detection performance (in fact it is optimal) as the separation between the pdf of clutter-only and the pdf of clutter-plus-target is the greatest among these three data formats used. The second best detection performance is found by using the amplitude data, and the log data does the worst. In the second case of $\nu = 1.0$ shown in Figure 3 the amplitude data performs best followed by the log data and the intensity. In the last case of $\nu = 0.5$ shown in Figure 4 the log data performs far better than the amplitude, and the intensity does a lot worse.



(a) Intensity

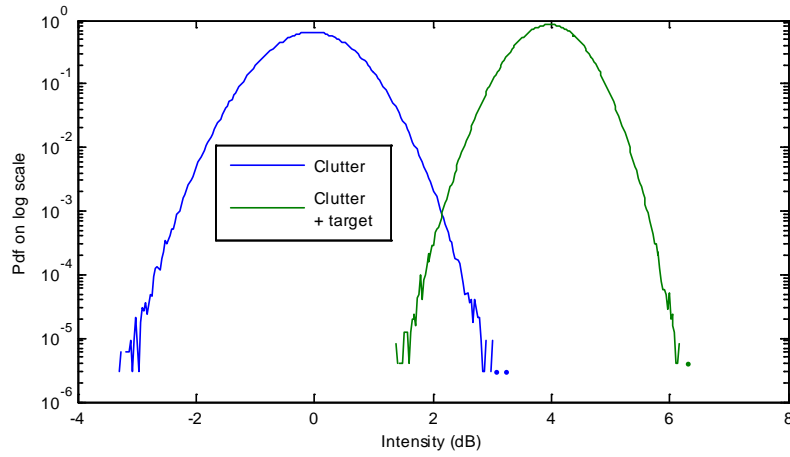


(b) Amplitude

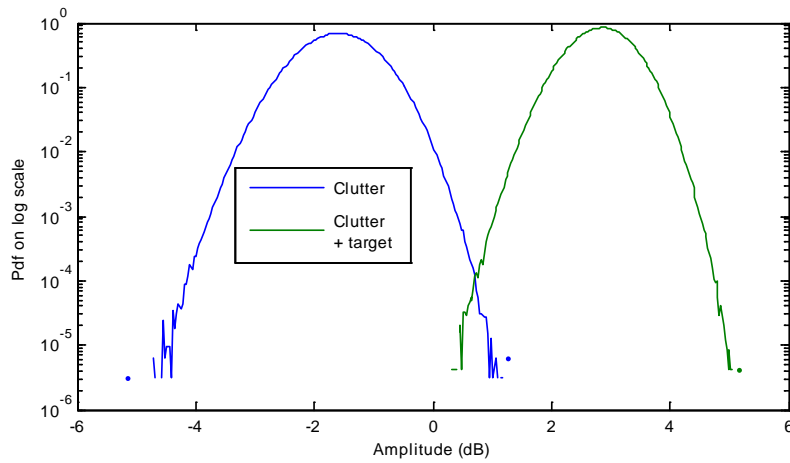


(c) Decibels

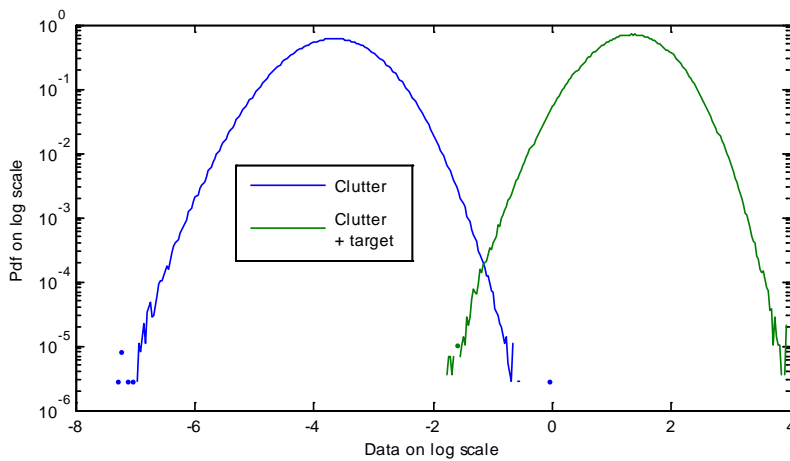
Figure 2: Empirical pdfs of clutter and clutter plus target ($\nu = \infty$, $\mu = 1.0$, $SCR = 1.5$ (1.76 dB) and $N = 100$) using three different quantities in non-coherent integration, namely, (a) intensity, (b) amplitude and (c) decibels.



(a) Intensity

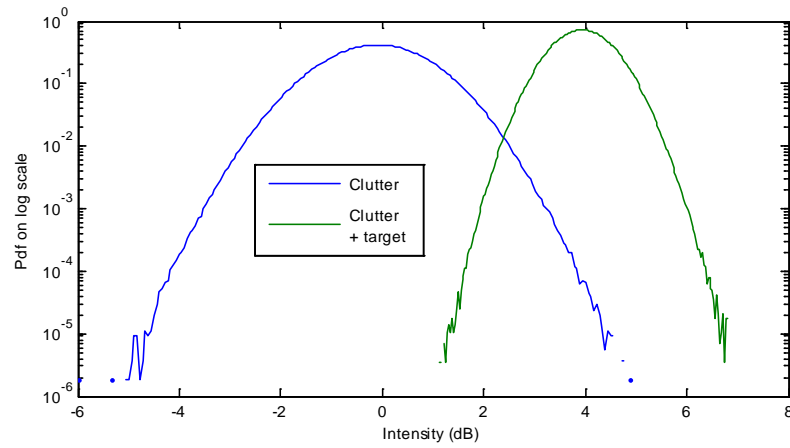


(b) Amplitude

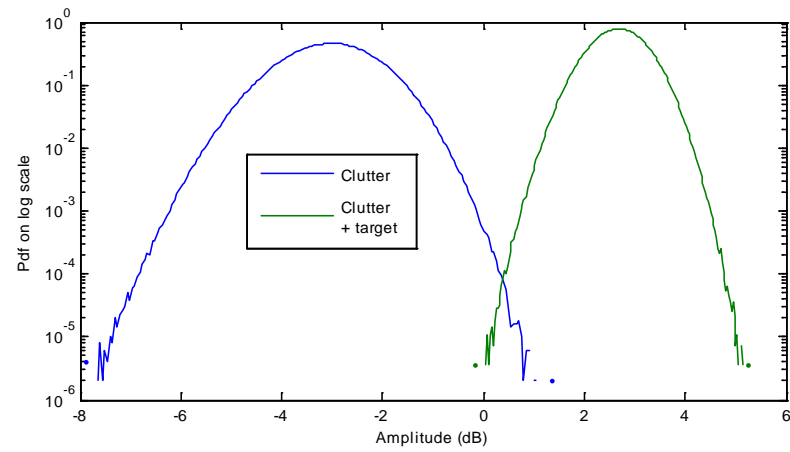


(c) Decibels

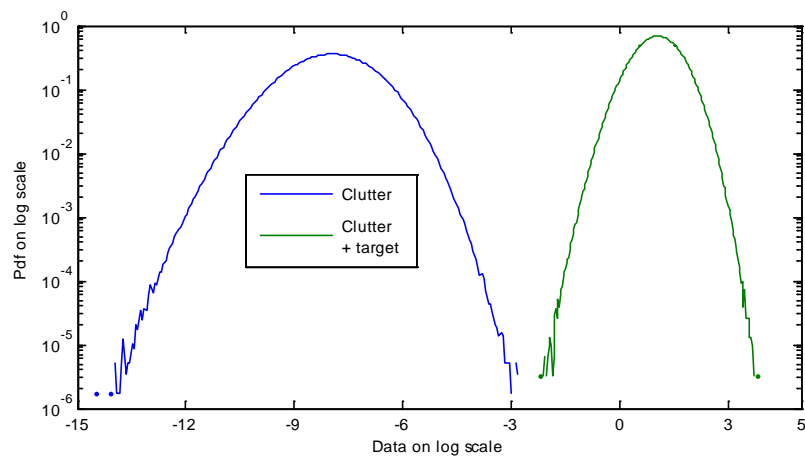
Figure 3: Empirical pdfs of clutter and clutter plus target ($\nu = 1.0$, $\mu = 1.0$, $SCR = 1.5$ (1.76 dB) and $N = 100$) using three different quantities in non-coherent integration, namely, (a) intensity, (b) amplitude and (c) decibels.



(a) Intensity



(b) Amplitude



(c) Decibels

Figure 4: Empirical pdfs of clutter and clutter plus target ($\nu = 0.5$, $\mu = 1.0$, $SCR = 1.5$ (1.76 dB) and $N = 100$) using three different quantities in non-coherent integration, namely, (a) intensity, (b) amplitude and (c) decibels.

Based on the above analysis, depending on the shape parameter, any of the three quantities tested can perform better than the others or vice versa. As a general rule of thumb, we suggest use of the following quantities for scan-to-scan non-coherent integration processing,

- Log data if $\nu \leq 1.0$
- Amplitude if $1 < \nu < 10$
- Intensity if $\nu > 10$

The challenge then becomes (a) to determine if sea clutter is K-distributed and (b) to estimate the shape parameter ν in real-time. Or alternatively, if sea clutter is found to be K-distributed, detectors could be run in parallel on all three quantities and the results are then fused to provide best detections. However, it is worth noting that sea clutter is not necessarily K-distributed.

4. Radon Transform and Radon Spectrum

The time elapsed for an acquisition of a scan-to-scan dataset is normally less than a minute, and for such a short period the velocity (speed and direction) of a slow moving target can be assumed to be constant, and hence its trace in a 2D range-scan radar image shall be a line event. The Radon transform is perhaps most powerful and useful in detecting line patterns in a noisy background. In this section we first briefly review the Radon transform and then introduce the Radon spectrum, analogous to the Doppler spectrum in radar coherent processing.

4.1 Radon Transform

The Radon transform was named after the Austrian mathematician, Johann Radon who introduced the transform in 1917. In the case of two dimensions, it is an integral transform consisting of the integral of a function over straight lines (Bracewell 1995, pp. 505-537). Mathematically, let $f(x, y)$ be a continuous function vanishing outside some large disc in the 2D Euclidean plane⁶. The Radon transform, R_f , is defined as the integral along a radial line (with a unit width) whose projection is defined by an orientation angle θ and a radius ρ .

$$R_f(\theta, \rho) = \int_{-\infty}^{\infty} \int_{-\infty}^{\infty} f(x, y) \delta(\rho - x \cos \theta - y \sin \theta) dx dy \quad (16)$$

⁶ For two-dimensional radar imagery, x may be the range bin number and y the scan number, or vice versa, and $f(x, y)$ the radar measurement (amplitude, intensity or log data etc).

where $\delta(\cdot)$ is the Dirac delta function. Interpretation of the Radon transform is shown in Figure 5, where $R_f(\theta, \rho)$ equals the integral of the shaded area on the image $f(x, y)$.

In the numerical implementation in Matlab, pixels in an image will be treated with a unit length in both row and column directions, and centred at $(\text{floor}((N_x + 1)/2), \text{floor}((N_y + 1)/2))$ for an image having $N_x \times N_y$ pixels. The orientation angle span is $0 \leq \theta < 180^\circ$ and the radius $-\sqrt{N_x^2 + N_y^2}/4 \leq \rho \leq \sqrt{N_x^2 + N_y^2}/4$. A point in the original image will be transformed to a sinusoidal curve in the Radon transformed image. The Radon transformed image is therefore a superposition of such $N_x \times N_y$ sinusoidal curves. Figure 6 shows the image of the Radon transformed $R_f(\theta, \rho)$ of an image $f(x, y)$ with a size of 200×300 pixels whose amplitudes obey a K-distribution of $\nu = 0.5$ and $\mu = 1.0$. It can be seen that there are some strong patterns in the Radon transformed image which will be explained and removed in the next subsection.

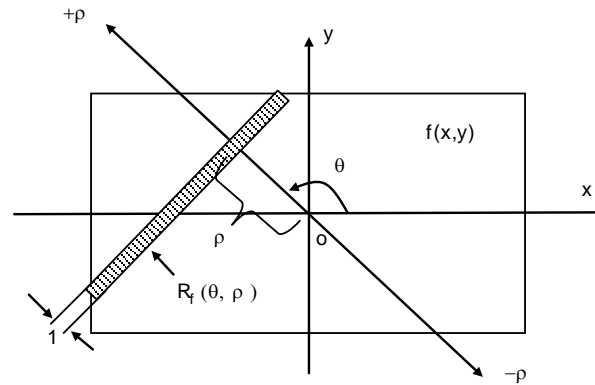


Figure 5: Interpretation of the Radon transform, the value of $R_f(\theta, \rho)$ is the integral along a unit width radial line whose projection is defined by a pair of coordinates (θ, ρ) .

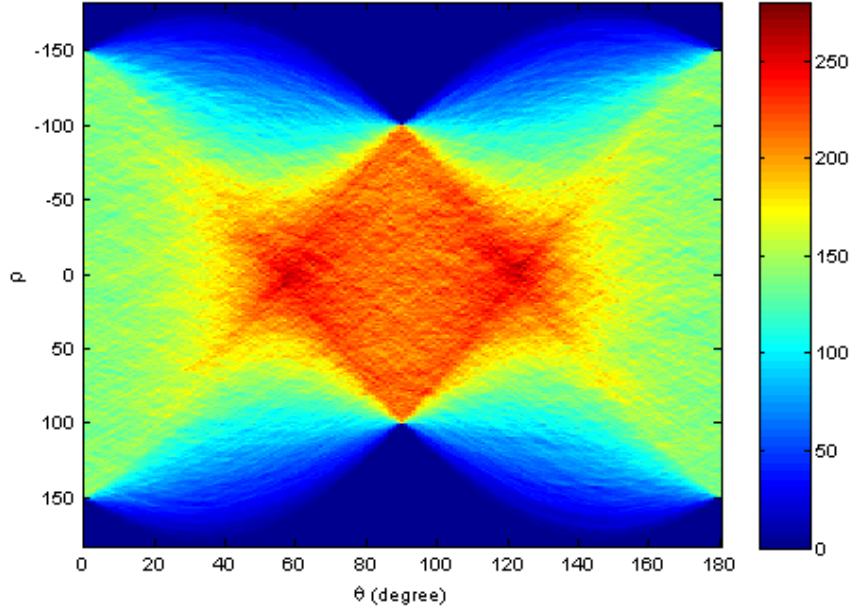


Figure 6: Radon transform of an image with a size of 200×300 pixels whose amplitudes obey a K-distribution of $\nu = 0.5$ and $\mu = 1.0$.

4.2 Radon Spectrum

The Radon transformed image of a textureless (i.e. featureless) image appears to have strong patterns as shown in Figure 6. This is caused by integral lengths that vary depending on the coordinates of (θ, ρ) . The maximum integration lengths are achieved at $\theta = \tan^{-1}(N_y / N_x)$ and $\rho = 0$, and symmetrically at $\theta = 180^\circ - \tan^{-1}(N_y / N_x)$ and $\rho = 0$ (the two paths that diagonally cross the image), hence resulting in two corresponding areas that have highest values. The valid region of ρ also depends on θ : $-N_y/2 \leq \rho \leq N_y/2$ for $\theta = 0, 180^\circ$ and $-N_x/2 \leq \rho \leq N_x/2$ for $\theta = 90^\circ$, for instance. The value of ρ achieves its maximum value of $\pm \sqrt{N_x^2 + N_y^2} / 4$ at $\theta = \tan^{-1}(N_y / N_x)$ and $\theta = 180^\circ - \tan^{-1}(N_y / N_x)$. Once ρ is out of its valid region, there is no data to support the integral, zero is assigned to the Radon transform. Therefore, some top portion and symmetrically the bottom portion of the Radon transformed image are in deep blue (zeros).

While the above pattern in the Radon transformed image is characteristic of the transform, it is not desirable for the purpose of radar detection. To remove patterns caused by variations in integration lengths, we normalise $R_f(\theta, \rho)$ by its integration length. The integration length for each path determined by the pair of (θ, ρ) may be calculated directly by the geometry. An alternative way is by the Radon transform of a matrix $I(x, y)$ that has the same dimensions of $f(x, y)$ and with all elements equal to one. The value $R_I(\theta, \rho)$ shall

equal the integration length of $R_f(\theta, \rho)$. The method of using $R_I(\theta, \rho)$ to normalise the Radon transform has also been discussed in a DSTO report (Jones et al. 2004). Therefore,

$$\bar{R}_f(\theta, \rho) = R_f(\theta, \rho) / R_I(\theta, \rho) \quad \text{if } R_I(\theta, \rho) \neq 0 \quad (17)$$

will be the normalised Radon transform. Elements of $R_I(\theta, \rho) = 0$ indicate ρ is out of its valid region and will be excluded in the normalisation. The image of the normalised Radon transform $\bar{R}_f(\theta, \rho)$ is shown in Figure 7. It can be seen that most features and patterns shown in Figure 6 disappear. However, it creates some new features in the top and bottom arc areas, due to short integration lengths.

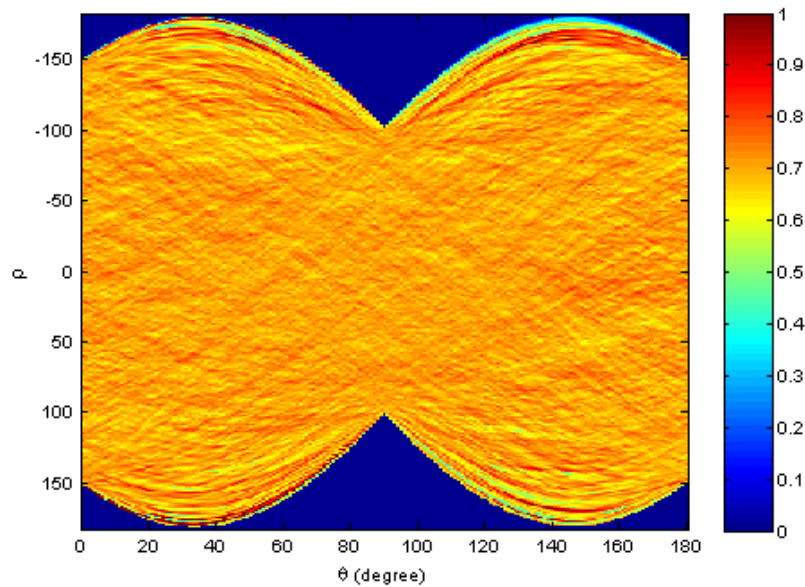


Figure 7: Image of the normalised Radon transform, $\bar{R}_f(\theta, \rho)$.

The normalised Radon transform is equivalent to an averaging process in all possible directions. The averaging processing along the column direction and row direction correspond to $\theta = 0$ and $\theta = 90^\circ$, respectively, and so on. For randomly distributed data, the variance (or the fluctuation of the data around its mean) depends on the number of samples (i.e. the length of the integration path in the Radon transform) used in the averaging processing. Since the integration lengths are relatively shorter for the top and bottom arc areas than the remainder, the fluctuation in these areas is certainly larger.

Non-coherent detection employs a multi-look averaging process to reduce the variance of clutter for detecting whether a target signal is embedded in the clutter. The number of multi-looks, which determines the reduction of the variance, is certainly an important parameter in the processing. Therefore, in the above normalised Radon transformed

matrix $\bar{R}(\theta, \rho)$, we further exclude those pixels whose integration length is shorter than the smaller of N_x and N_y , i.e.,

$$\bar{\bar{R}}_f(\theta, \rho) = \begin{cases} R_f(\theta, \rho) / R_I(\theta, \rho) & R_I(\theta, \rho) \geq \min\{N_x, N_y\} \\ 0 & \text{elsewhere} \end{cases} \quad (18)$$

We call Equation (18) the 2D Radon spectrum of image $f(x, y)$. Each non-zero pixel of the Radon spectrum is equal to the average value along a specifically tilting line in the image. The minimum number of the multi-look is $\min\{N_x, N_y\}$ which also determines the worst variance of the Radon spectrum⁷.

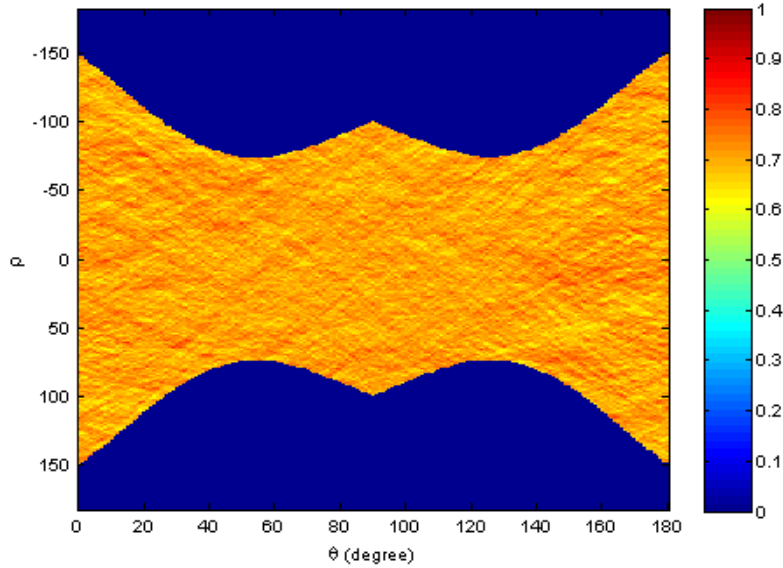


Figure 8: 2D Radon spectrum of an image $f(x, y)$ with a total of 200×300 pixels obeying a K-distribution of $\nu = 0.5$ and $\mu = 1.0$.

For a K-distribution with $\nu = 0.5$, the distribution after amplitude⁸ multi-look averaging processing is given by (9), from which we can compute the threshold T_N for a given false-alarm rate P_{faN} , by,

$$P_{faN} = \int_{T_N}^{\infty} P_N(t) dt = \Gamma_{inc}(N, cNT_N) / \Gamma(N) \quad (19)$$

⁷ This means that any tilting lines that are shorter than $\min\{N_x, N_y\}$ are not included in the Radon spectrum, i.e., target traces along these lines will not be considered in the detection process.

⁸ It was shown earlier that for K-distributed data with $\nu = 0.5$, one should use the log format for a better detection performance. The use of amplitude here is for demonstration as its threshold can be theoretically determined.

where $\Gamma_{inc}(a, z) = \int_z^\infty t^{a-1} e^{-t} dt$ is the incomplete Gamma function⁹

Suppose we require a false-alarm rate of $P_{fa} = 10^{-6}$ for the original data, therefore after non-coherent multi-look integration the false-alarm rate becomes,

$$P_{faN} = NP_{fa} \quad (20)$$

where $N = \min\{N_x, N_y\}$, and $N = 200$ for this example.

The 2D Radon Spectrum shown in Figure 8 is re-plotted as a 1D spectrum against the orientation angle θ in Figure 9. In addition, three red-lines are also drawn to show the mean of the Radon spectrum (i.e. the mean of clutter amplitude, $\bar{t} = 1/c$ in dB shown as the thick red-line), the threshold corresponding to $P_{faN} = 2 \times 10^{-4}$ ($P_{fa} = 10^{-6}$, the solid red-line) and the threshold corresponding to $P_{faN} = 2 \times 10^{-3}$ ($P_{fa} = 10^{-5}$, the broken red-line), respectively.

Theoretically, for the given false-alarm rates, the expected numbers of false-alarms should be 0.06 for $P_{faN} = 2 \times 10^{-4}$ ($P_{fa} = 10^{-6}$) and 0.6 for $P_{faN} = 2 \times 10^{-3}$ ($P_{fa} = 10^{-5}$), respectively. In fact we can see from Figure 9 that there are no false-alarms for $P_{faN} = 2 \times 10^{-4}$ but one for $P_{faN} = 2 \times 10^{-3}$ in this case.

We can also observe that the fluctuation of the Radon spectrum is slightly larger at the two ends (the neighbourhood of $\theta = 0$ and 180°) than the central areas. This is because at the ends the number of samples used in the multi-look averaging processing is the smallest, compared to the other parts. It is known for the given distribution that the standard deviation equals $\sigma_N = \bar{t} / \sqrt{N}$, where N is the number used in the multi-look averaging processing. The smaller the number of multi-looks, the larger the variance and hence the fluctuation.

The threshold shown in Figure 9 is determined using the smallest number of multi-look samples. Since the number of multi-look samples varies with the orientation θ , and for the correlated sea clutter, the amount of correlation largely depends on the wind / wave direction, ideally, the threshold should also varies with the orientation. This is discussed and applied in the following section.

⁹ In Matlab the incomplete Gamma function is defined as, $\Gamma_{inc}(z, a) = \frac{1}{\Gamma(a)} \int_0^z t^{a-1} e^{-t} dt$. Therefore,

using the Matlab's definition, (19) should be written as, $P_{faN} = \int_{T_N}^\infty P_N(t) dt = 1 - \Gamma_{inc}(cNT, N)$.

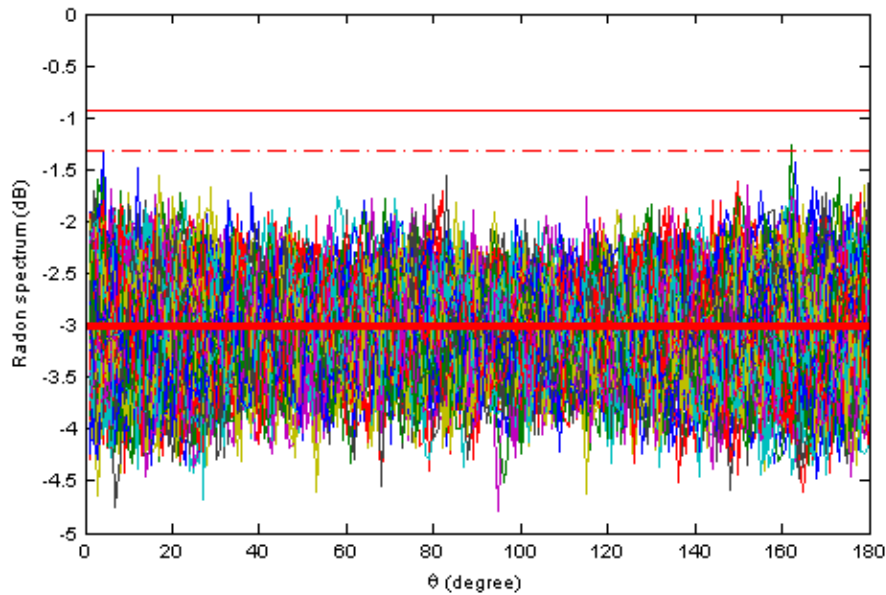


Figure 9: Radon spectrum against orientation angle. The thick red-line is the mean of the spectrum (the mean amplitude of clutter), the solid and broken red-lines are the thresholds corresponding to $P_{faN} = 2 \times 10^{-4}$ ($P_{fa} = 10^{-6}$) and $P_{faN} = 2 \times 10^{-3}$ ($P_{fa} = 10^{-5}$), respectively.

After introducing the concept of the Radon Spectrum, not only is the 2D Radon spectrum shown in Figure 8 visually very similar to a range-Doppler map for coherent detection processing, but the processing to follow is also the same. Once a pixel of $\bar{\bar{R}}_f(\theta, \rho)$ exceeds a pre-determined threshold, target presence may be declared. The location of the target trace in the range-scan image is then determined by (θ, ρ) , which indicates the range and velocity.

Implementation of the Radon transform in digital signal processing may be through the fast Fourier transform (Jones et al. 2004). Therefore, the computational cost for computing the Radon spectrum might be similar to the cost for computing the Doppler spectrum in coherent multi-look processing. How to implement fast calculation of the Radon spectrum is out of scope for this report, and may be a topic for the future research.

5. Examples

In this section we present four examples to show the use of the Radon spectrum for detecting range-bin shifted weak target signals embedded in sea clutter.

5.1 A Simulated Case

A 2D 256×500 dataset was generated representing a range-scan K-distributed sea clutter dataset with a shape parameter of $\nu = 0.5$. A moving Swerling I target with a SCR of 4 dB was also embedded, and was made to appear in the period from scan 50 to scan 200 (i.e. 30 seconds). Under the assumption of a scan rate of 300 rpm and a range resolution of 1m, the moving target has a radial velocity of 3.58 m/s (or 6.96 knots). Figure 10 shows the range-scan image of the data in which a trace of the moving target is barely visible.

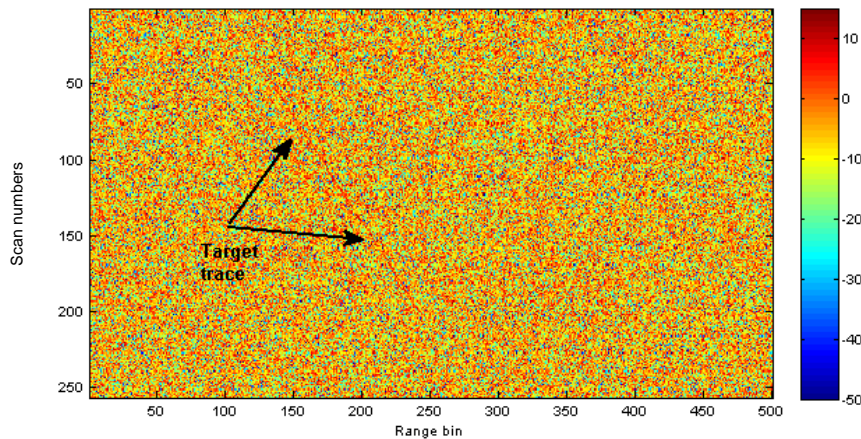


Figure 10: A weak target trace appears in the range-scan image.

For such a weak target signal trace, it is impossible to detect if the detection scheme is based on pixel based processing. Figure 11 shows threshold exceedances based on the pixel based processing with a false-alarm rate of 5%. It can be seen that the trace of the target is hardly identified even with such a high false-alarm rate. Therefore, any high false-alarm rate track-before-detect scheme will fail if the processing is based on this kind of approach.

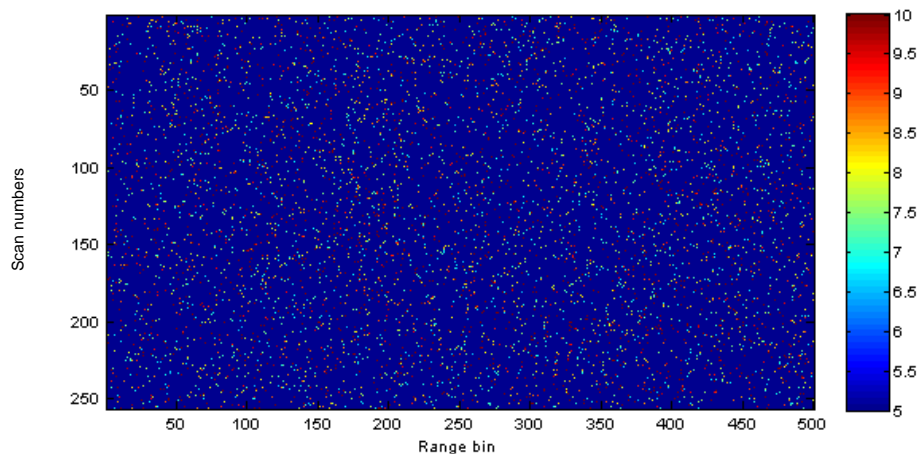


Figure 11: Pixel based detects with a false-alarm rate of 5%.

The 2D and 1D Radon spectra of the image are shown in Figure 12 and Figure 13, respectively. From these one can see that the embedded target signal has been robustly detected without giving any false-alarms for a desired false-alarm rate of $P_{fa} = 10^{-6}$. As discussed in Section 3, for a K-distributed dataset with a shape value of $\nu = 0.5$, the log data provides the best performance for non-coherent multi-look integration processing. Therefore, the data in its log format was used in the Radon transform processing. The detection threshold shown in Figure 13 was numerically calculated from the Monte Carlo simulation, as the distribution of the multi-look K-distributed data in the log format has no closed-form.

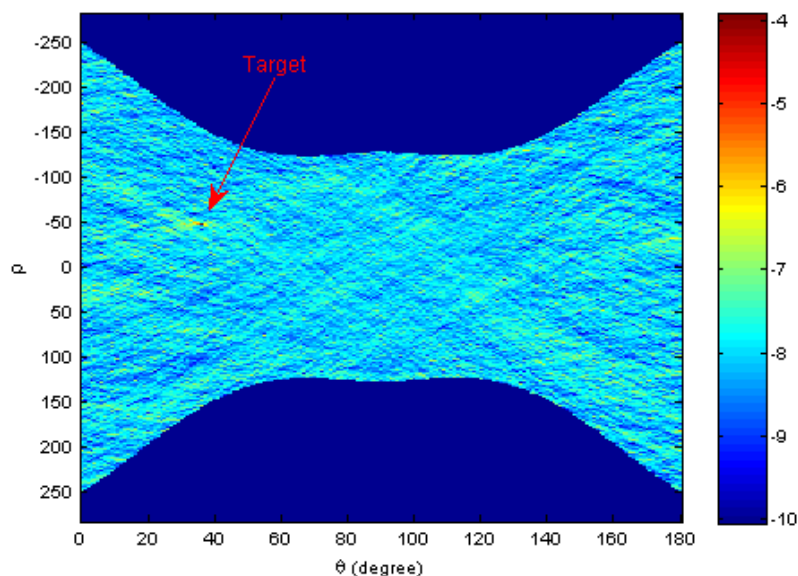


Figure 12: 2D Radon spectrum of the simulated range-scan dataset showing the detection of the target.

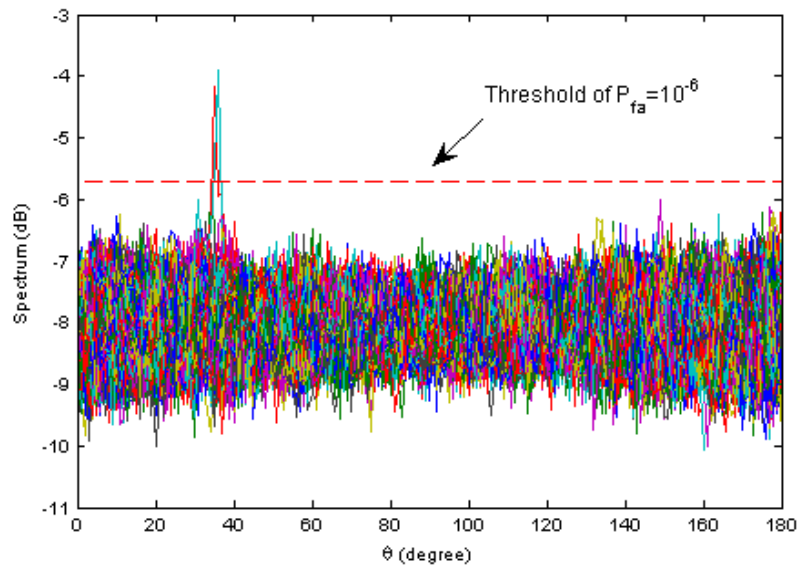


Figure 13: 1D Radon spectrum of the simulated range-scan dataset using the log format. The target trace is robustly detected with no false-alarms at a given false-alarm rate of $P_{fa} = 10^{-6}$.

The 1D Radon spectra using the quantities of amplitude and intensity are shown in Figure 14 and Figure 15, respectively. Together with Figure 13, we can see that the log data results in the best detection performance, followed by the amplitude, and the intensity performs the worst, which is consistent with the previous analysis presented in Section 3.

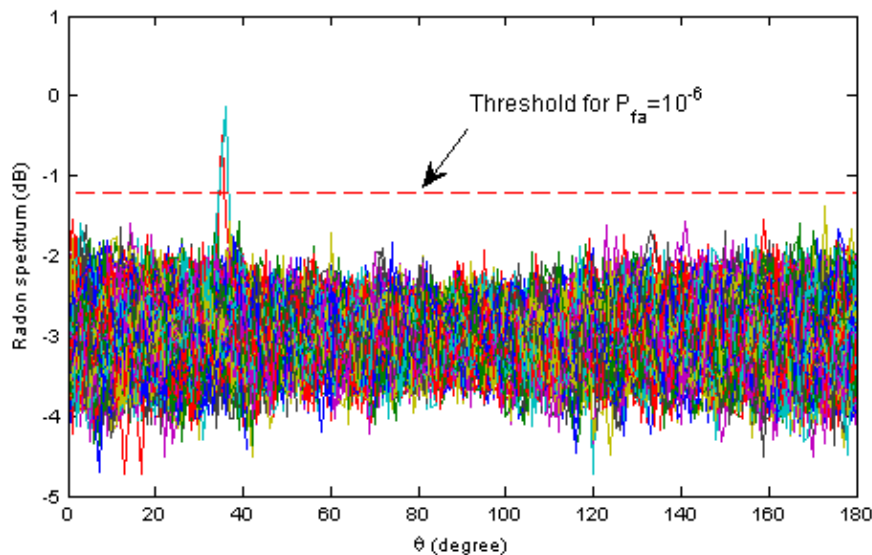


Figure 14: 1D Radon spectrum of the simulated dataset and the associated threshold, using amplitude in the process.

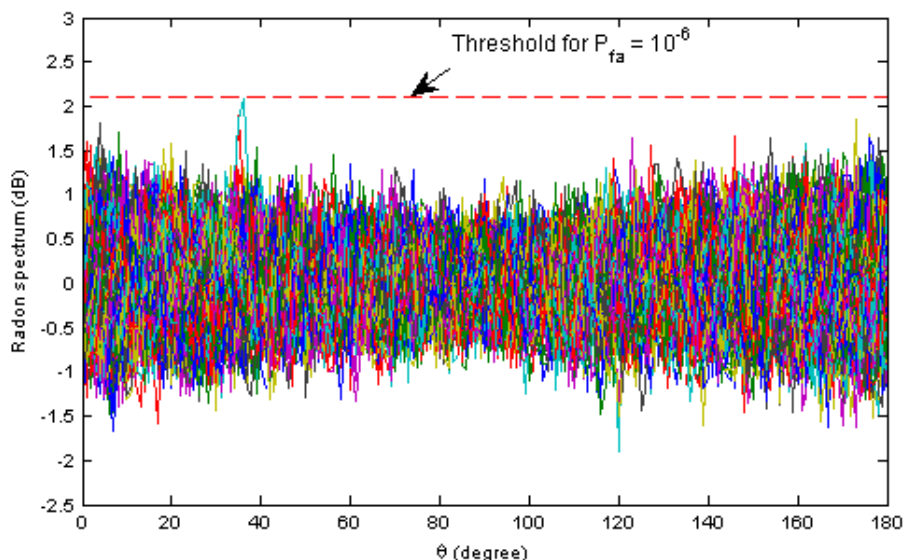


Figure 15: 1D Radon spectrum of the simulated dataset and the associated threshold, using intensity in the process.

There is a processing loss that occurs when the tilt angle of a line pattern we want to detect is not perfectly perpendicular to the projection lines in the Radon transform. The tilt angle of a line pattern in the image can be any value, but the angle resolution used in the Radon transform for numerical calculations is limited. A finer resolution for the Radon transform may be chosen if computational cost is not a concern. When the angle of a tilted line does not exactly equal the orientation angle used by Radon transform, the integration cannot include all energy from the target, therefore a processing loss is unavoidable. This is analogous to the Doppler spectrum analysis in coherent processing. A target can have any Doppler frequency, but the resolution of the numerically calculated Doppler spectrum is limited. A processing loss occurs once the target's Doppler frequency is not a multiple fold of the frequency resolution used in the Fourier transform. The point here is to find what the loss is likely to be in the Radon spectrum. In fact in the above example, the velocity of the moving target was purposely chosen so that the angle of its range trace tilts 35.5° from vertical, one of the worst cases for the Radon transform using one-degree resolution from 0 to 180 degrees. To retrieve the loss, the Radon spectrum is re-calculated using a half-degree resolution, so the projection at 35.5° was also included. The resulting Radon spectrum is shown in Figure 16. It can be seen compared to Figure 13 that the peak of the target signal increases by about 0.7 dB. Alternatively, we may conclude that the maximum loss for the Radon transform using a one-degree resolution for the image used in the test is less than 1 dB.

A target trace not in a perfectly rectilinear fashion in the range-time image results in another integration loss. The cause can be manifold. For instance, a target with non-constant velocity (i.e. speed and/or direction variations) will leave a nonlinear trace in the range-time image. Sometimes even both the target and radar platform have constant velocities, the target trace in the range-time image can be non-rectilinear (a case of which is

shown in Subsection 5.4). While target motion is uncontrollable, if the radar intends to use the Radon spectrum for non-coherent detection, it needs to use a proper range reference system, so that moving targets with constant velocities will leave rectilinear trajectories in the 2D image to be processed. If target trajectories in the image are straight lines, the longer the integration time, the better the detection. However, if the trajectory is not rectilinear, the target energy spreads in the Radon spectrum, and using a longer integration time may deteriorate detection. This is because for a nonlinear trajectory, each integral along a particular straight line can only include a part or parts of the nonlinear trajectory (the tangent part). For such cases, using shorter integration may result in better detections. A further discussion is presented in Subsection 5.4.

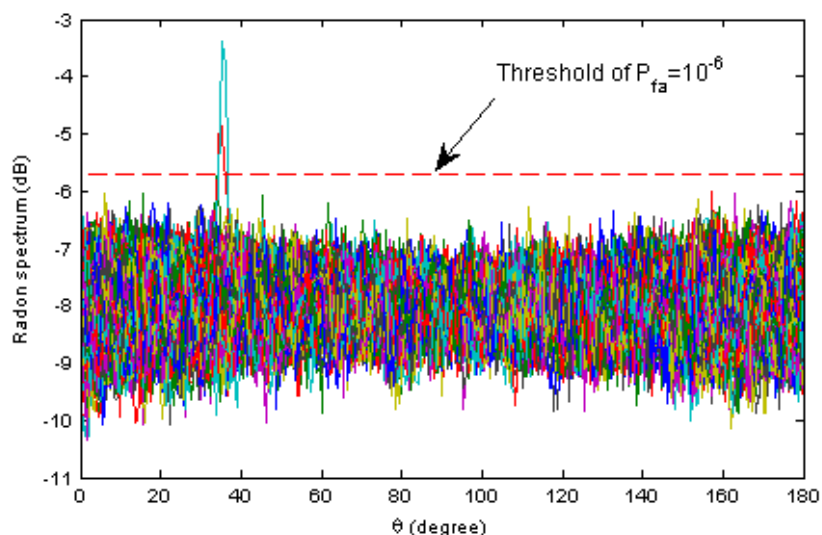


Figure 16: Radon spectrum uses a half-degree resolution so that the tilt angle of the target trace is exactly perpendicular to one of the projection lines in the Radon transform. Target peak increases 0.7 dB compared to the Radon spectrum with a one-degree resolution.

5.2 Christmas Island S-band Data

The scan-to-scan data collected by the Kelvin Hughes S-band ‘SharpEye’ radar were used here as a case study. Specifically the dataset was collected from a trial on Christmas Island, an Australian territory in the Indian Ocean. The radar was mounted on a tower overlooking the sea on the 7th May 2013 (dataset name: ‘130507_missed’). Parameters of the radar are given in Table 1.

The Kelvin Hughes S-band ‘SharpEye’ radar has a complex waveform. Each ‘pulse’ is a combined pulse and really a triplet of pulses: a short pulse that is not compressed, a medium pulse and a long pulse both of which are compressed to 15 metre range resolution. The long pulse data is used to cover the long range region, and where in the short range region it has significant eclipsing losses, the medium pulse data is used. Where the medium pulse data is significantly eclipsed, then the short pulse data is used. The three sets of data are digitally combined, but this generates boundaries in the data at

(about) range bin 180 and range bin 680. The data from each pulse is then combined into a table with the prior 16 or 32 combined pulses (depending upon use of 48 or 24 nautical mile mode) and Fourier transformed. The Fourier transformed data is then CFAR processed (believed to be range only) and the signal to CFAR level computed for each Doppler bin (generating 16 or 32 values). The output video return is believed to be determined by the largest signal to CFAR value for each range bin (every range bin generates a return, and it is not so much a threshold as a data selection rule). A return is generated for every triplet transmitted with the data from that triplet rotating through the FFT table. The video signal is log scaled on a 0-to-1 volt scale. In the capture process, the 0-to-1 volt output is digitised to 0 to 255 (one byte) levels. A typical range profile collected by a combined pulse is shown in Figure 17. The boundary between the short and medium pulses at about range bin 180 and the boundary between the medium and long pulses at about range bin 680 are clearly seen. Because of the compensation treatment, the data can be considered to be independent of range, especially beyond range bin 1500.

Table 1: Parameters of the Kelvin Hughes S-band 'SharpEye' radar.

Parameter	Value
Carrier frequency	2.95 GHz
Polarisation	HH
Peak power	≥ 170 w
Azimuth beamwidth	$\leq 1.9^\circ$
Elevation beamwidth	$\approx 26^\circ$
Range resolution (after pulse compression)	15 m
Scan rate	24 rpm
Number of returns per scan	3073
Waveform repetition frequency	1227 Hz
Number of range bins per 'combined pulse'	6000

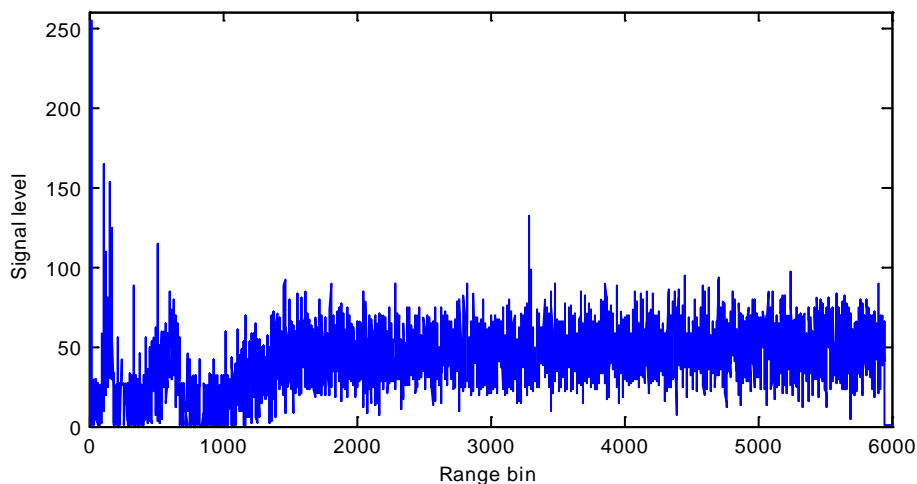


Figure 17: A typical range profile collected by a pulse (dataset name 130507_missed, scan number 4200 and pulse number 881).

The empirical pdf of homogeneous sea clutter ranging from bin 2000 to bin 5900 is plotted in Figure 18, which was obtained using over one million samples. Between the two distributions (namely, the normal distribution and the Gamma distribution) used to fit the data, the normal distribution seems to fit better, possibly because the data is in the logarithmic form. Spikes on the empirical pdf are believed to be the artificial effects of quantisation when the analogue output is scaled to 0-255 levels. The data distribution shows a 'flat' tail on the log scale (the bottom plot) which is possibly resulted by the data processing carried out by the radar described earlier.

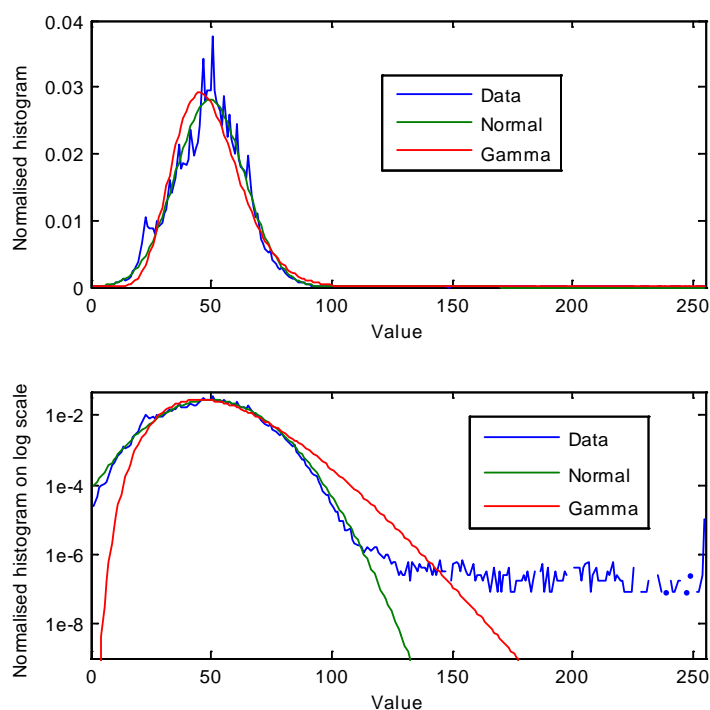


Figure 18: Distributions of sea clutter collected by the Kelvin Hughes S-band 'SharpEye' radar.

For the case study, the dataset was manually inspected and two scan-to-scan subsets each containing a 'small' target were extracted and are shown in Figure 19 and Figure 20, respectively. The corresponding pulses for Target 1 (Figure 19) and Target 2 (Figure 20) were 891 and 1481, respectively. Since the antenna was constantly rotating, different pulses corresponded to different search directions. Because Target 1 occupied about two to three range bins and Target 2 about one to two range bins, for the 15m range resolution, they were indeed small targets in the maritime environment. Both traces showed very good linearity, indicating they travelled with constant speeds during the data collection period. According to the slopes of the traces, their radial velocities were 8.9 m/s (17.3 knots) and -3.9 m/s (-7.6 knots), respectively.

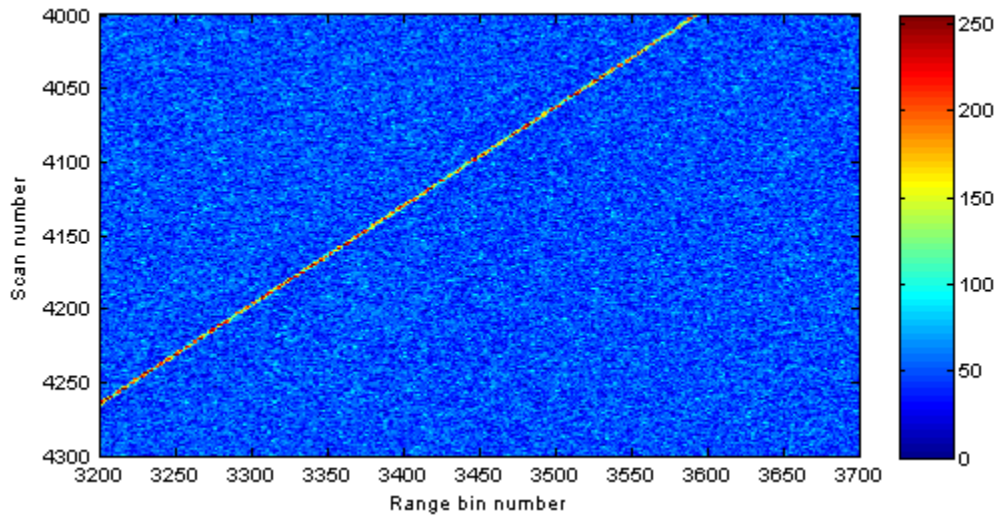


Figure 19: A target ('Target 1') trace shown in the range-scan image (dataset name: 130507_missed and pulse number: 891).

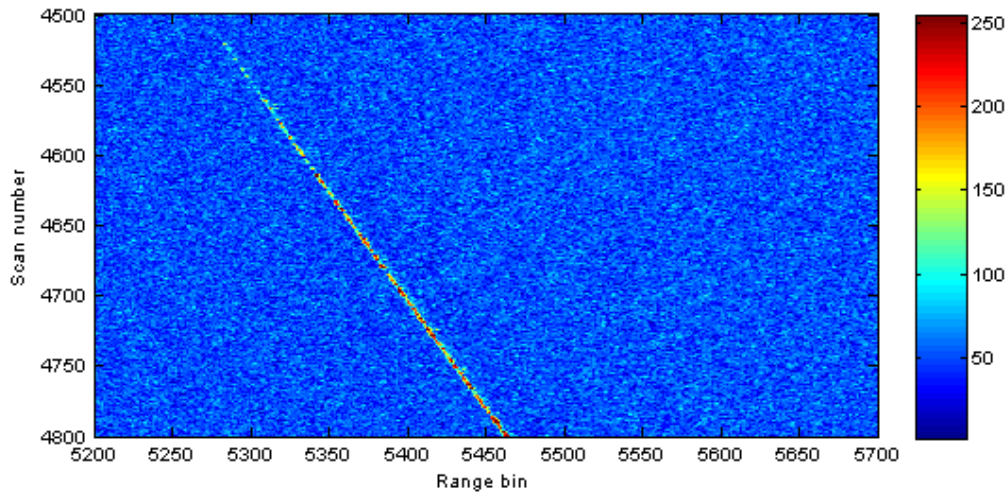


Figure 20: A target ('Target 2') trace shown in the range-scan image (dataset name 130507_missed and pulse number 1481).

These two targets might be physically small but not small enough, and their radar returns were strong compared to the background. Therefore, the conventional track-before-detect or other detection schemes would be sufficient for detecting such targets. In order to test the performance of the proposed algorithm, weak target traces are preferred. In doing so, we fabricated a weak target by placing Target 1 in the radar's sidelobe direction rather than the mainlobe direction. For a scanning radar, if its mainlobe steers at the target for the current pulse, it will gradually steer away from the target for the following pulses. Figure 21 shows a barely-seen trace of Target 1 captured by the radar's sidelobe using

pulse 918, (27 pulses after the mainlobe pulse). We call this associated target a weak target in order to distinguish between the two.

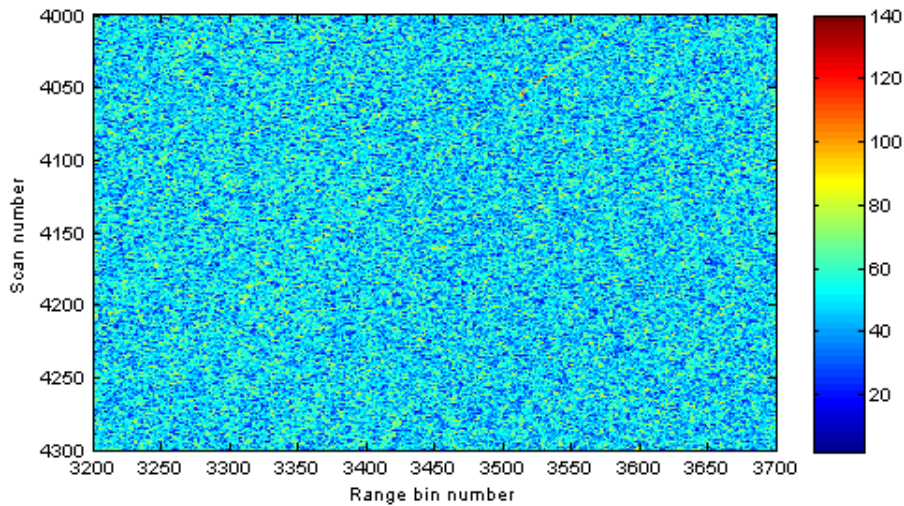


Figure 21: A 'weak target' was fabricated by steering the mainlobe away from the target, so the target was captured by the radar's sidelobe (dataset name: 130507_missed and pulse number: 918).

The detection of the weak target using conventional detection schemes, such as track-before-detect, is difficult. For instance, the pixel-based detects from the subset containing the weak target with a false-alarm rate of 10^{-2} is shown in Figure 22 where no obvious trace of the weak target is seen.

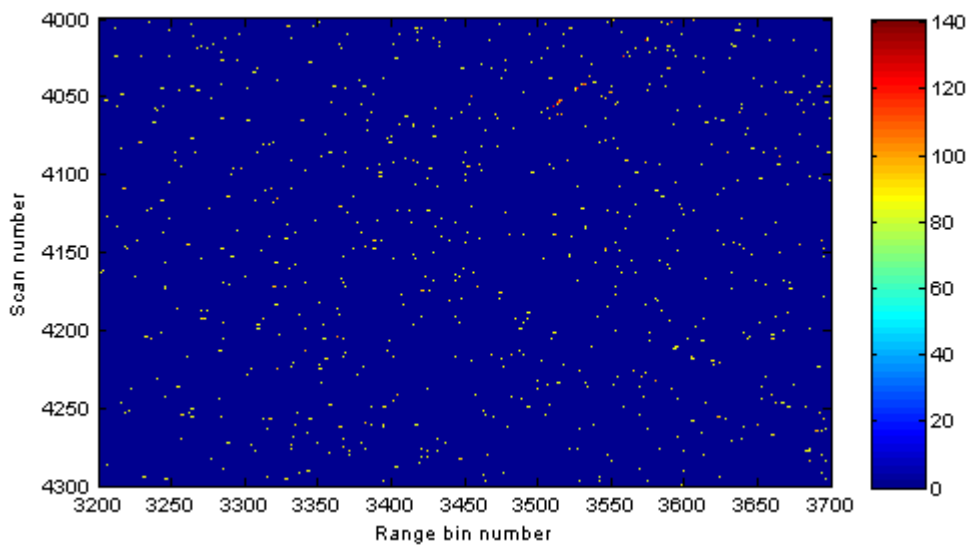
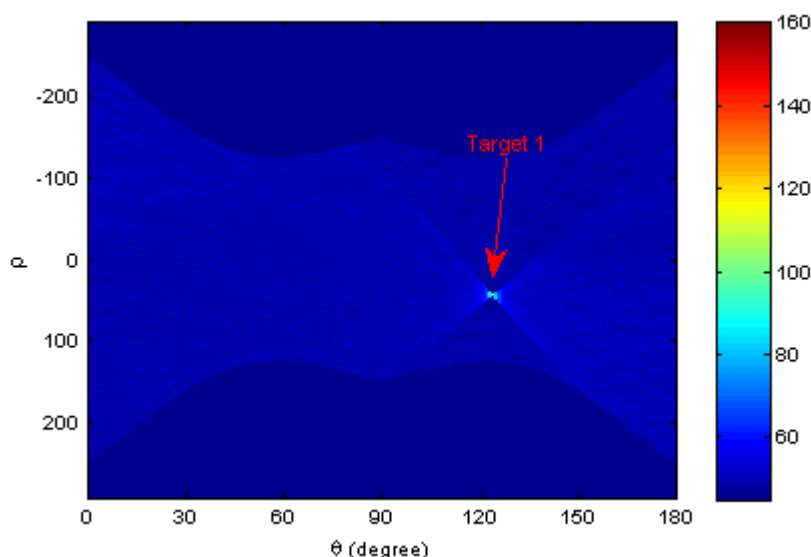
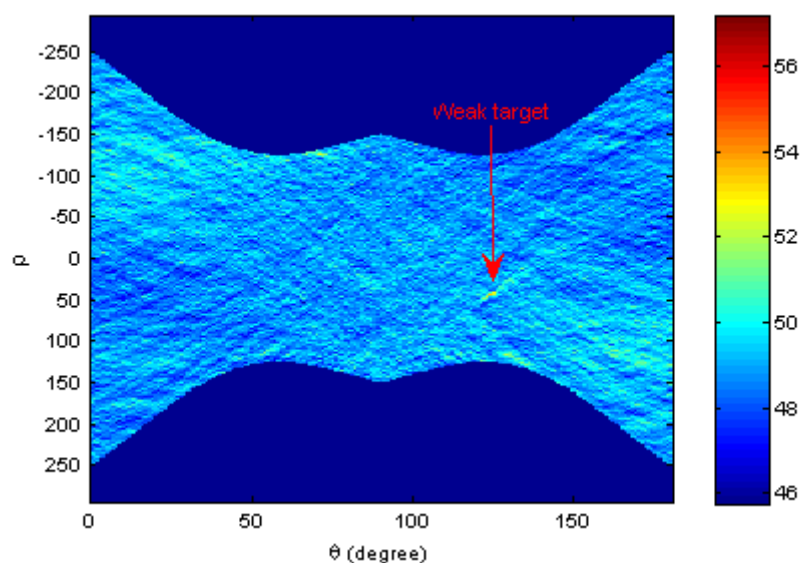


Figure 22: Pixel-based detects from the subset containing the weak target with a false-alarm rate of 10^{-2} .

Comparisons of 2D and 1D Radon spectra associated to subsets containing Target 1 and the weak target are shown in Figure 23 and Figure 24, respectively. The associated threshold for a false-alarm rate of $P_{fa} = 10^{-6}$ is also shown, indicating that the weak target can be robustly detected using the Radon spectrum. Interestingly, there are excessive false-alarms for both datasets than there should be for the calculated threshold. This is due to the fact that the threshold was calculated based upon the assumption of the clutter data being normally distributed. However, the actual distribution of the data has a flat tail (see Figure 18), well departed from the assumed fitting, resulting in a relatively conservative threshold.

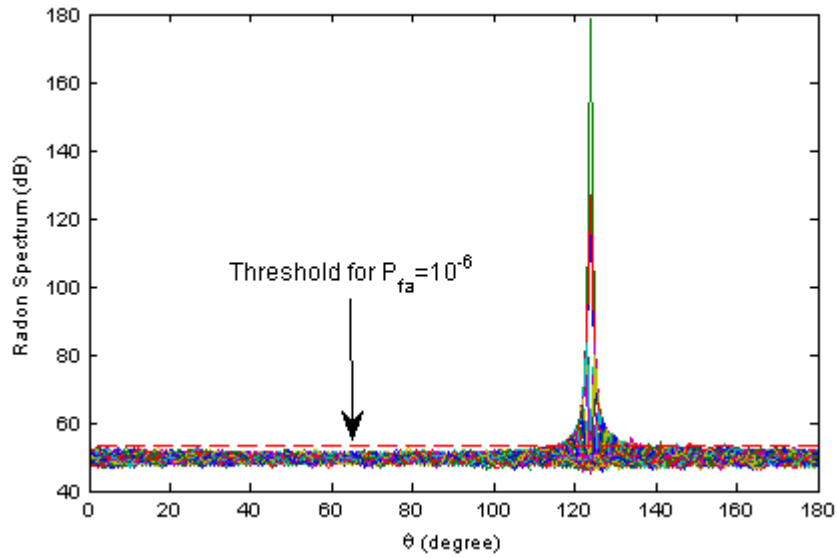


(a) 2D Radon spectrum of the subset containing Target 1

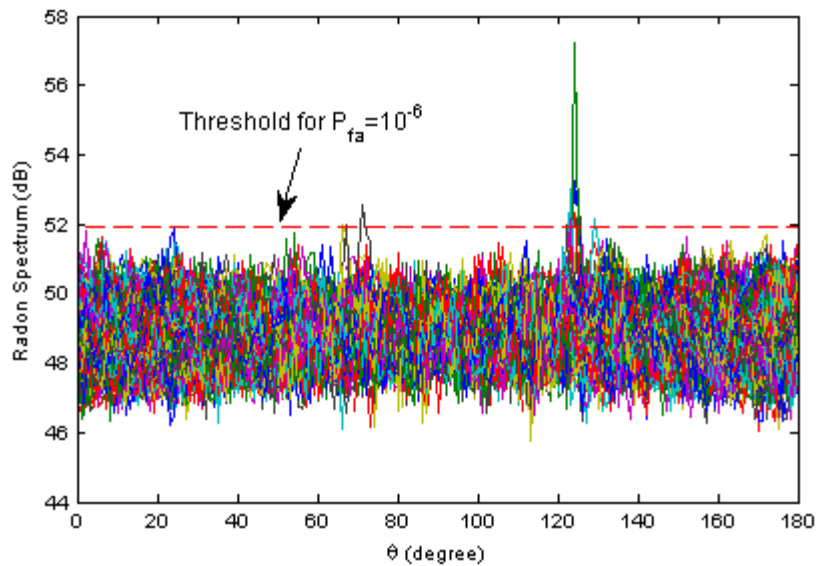


(b) 2D Radon spectrum of the subset containing the weak target

Figure 23: Comparison of 2D Radon spectra of the subsets containing Target 1 and its companion weak target.



(a) 1D Radon spectrum of Target 1



(b) 1D Radon spectrum of the weak target

Figure 24: Comparison of 1D Radon spectra of data subsets containing Target 1 and its companion weak target. The threshold for $P_{fa}=10^{-6}$ is shown, assuming data to be lognormal distribution.

5.3 X-band Data

In this section we look at two other real radar datasets collected from a stationary cliff-top radar, one without target and the other with a moving target collected over the sea surface. Some radar parameters are given in Table 2.

Table 2: Radar parameters for sample X-band data

Parameter	Value
Carrier centre frequency	9.76 GHz
Polarisation	VV
Range resolution	0.3 m
Range	5.5 km
Scan rate / pulse repetition frequency [#]	2400 rpm / 40 Hz
Number of scans / pulses	240
Number of range bins	256

[#] The original data was collected with a PRF of 1000 Hz. The data was down sampled to a PRF of 40 Hz, or equivalently, 2400 rpm.

5.3.1 Sea Clutter Only Dataset

Figure 25 shows the image of sea clutter only data in which the DC component was removed and the data was normalised to zero for the log data (note that this normalisation is not equivalent to normalising the intensity to 1). It is evident that the sea surface was very rough, making the sea clutter very spiky. Both the K- and lognormal distributions were fit the data's distribution however neither of them provided a satisfactory result. The empirical pdf of the data and the two approximated distributions are shown in Figure 26. While both the approximated distributions do not fit the data very well, the lognormal fit does much better in the tail region, possibly due to patches of sea swells (spikes) seen in the image.

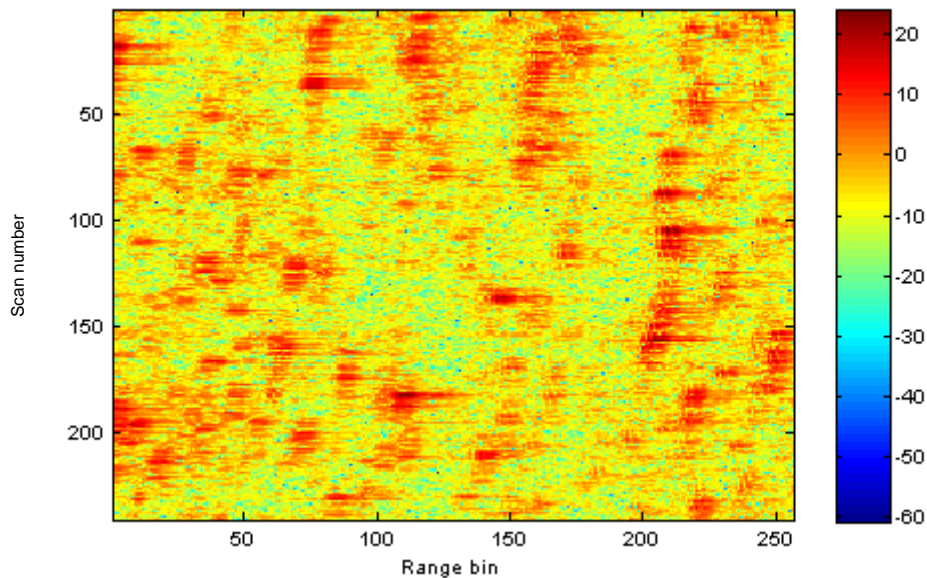


Figure 25: Image of range-scan radar sea clutter.

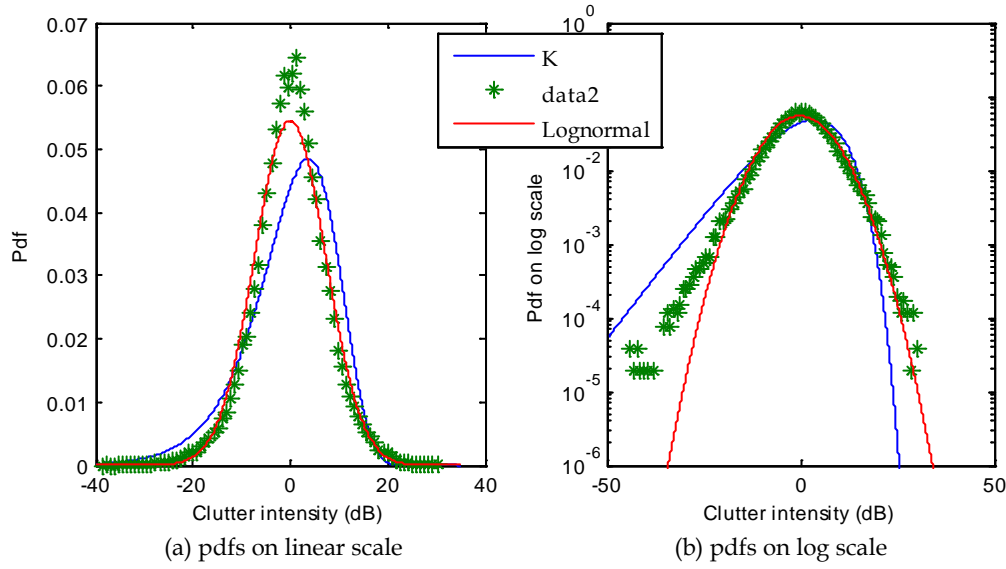


Figure 26: Empirical pdf of the data with the fit of K- and lognormal distributions.

In the following processing, we assumed that the data have a lognormal distribution, i.e. data in the log format be normally distributed.

Our next step is to determine the threshold for a given false-alarm rate. For a normal distribution, the threshold q_T for a given false-alarm rate P_{fa} can be determined by the cdf of the normal distribution, as,

$$P_{fa} = P(q > q_T) = \frac{1}{2} \left(1 - \operatorname{erf} \left(\frac{q_T - \bar{q}}{\sqrt{2\sigma_q^2}} \right) \right) \quad (21)$$

where $q = 10 \log_{10}(z)$ is the data in log format and q has a normal distribution, $\bar{q} = E\{q\}$ and $\sigma_q^2 = \operatorname{var}\{q\}$.

The mean of multi-look data (in log format) is still normally distributed, and if there is no correlation, the variance of multi-look data should be reduced by the number of multi-looks, N . However, when data is correlated, the equivalent number of multi-looks reduces. By viewing the image shown in Figure 25, strong correlation in both the fast-time domain (i.e. in the row direction, range bin to range bin) and the slow-time domain (i.e. in the column direction, scan to scan) is apparent. Variance of the original single-look data and variances of multi-look in column and row are given in Table 3. Viewing Figure 25, it seems that the correlation along tilting lines is not as strong as the correlation along horizontal rows.

Table 3: Original variance and variances after multi-look averaging in column and row for the sea clutter dataset in log format.

Data	Number of looks	Variance	Equivalent number of looks
Original data	1	53.47	1
Averaging in scan	240	2.40	22.3
Averaging in range	256	2.41	22.2

It can be seen that the equivalent numbers of multi-looks differ significantly from the actual number of looks used in the averaging processing because of correlation. For uncorrelated data having a normal distribution, the variance of multi-look data is given by,

$$\sigma_{qN}^2 = \sigma_q^2 / N \quad (22)$$

where N is the number of multi-looks. For correlated data, N should be replaced by N_{eq} , the equivalent number of looks, when calculating the threshold for the correlated data, as,

$$P_{faN} = P(q > q_T) = \frac{1}{2} \left(1 - \operatorname{erf} \left(\frac{q_T - \bar{q}}{\sqrt{2\sigma_q^2 / N_{eq}}} \right) \right) \quad (23)$$

The 2D Radon spectrum of the data is shown in Figure 27. Since the data has high correlation in row and column directions, its Radon spectrum shows patches with high values at $\theta = 0, 180^\circ$ and $\theta = 90^\circ$ areas. Appearing in the spectrum are also quite a few sinusoidal curve patterns that result from strong points in the range-scan image. The 1D Radon spectrum is plotted in Figure 28 where a threshold for $P_{fa} = 10^{-6}$ calculated by (23) is also drawn, and no false-alarms occur. The value of N_{eq} used was the smaller one of the equivalent numbers of multi-look in column or row. The data is heavily correlated which results in a much smaller equivalent number of looks in the multi-look averaging processing. As a consequence, the variance of the multi-look data is still relatively large (compared to that of non-correlated data) leading to a relatively high threshold. The threshold for this example is 5.3 dB. In another words, if there is a target trace in a line pattern with a SCR great than 5.3 dB, then it is detectable.

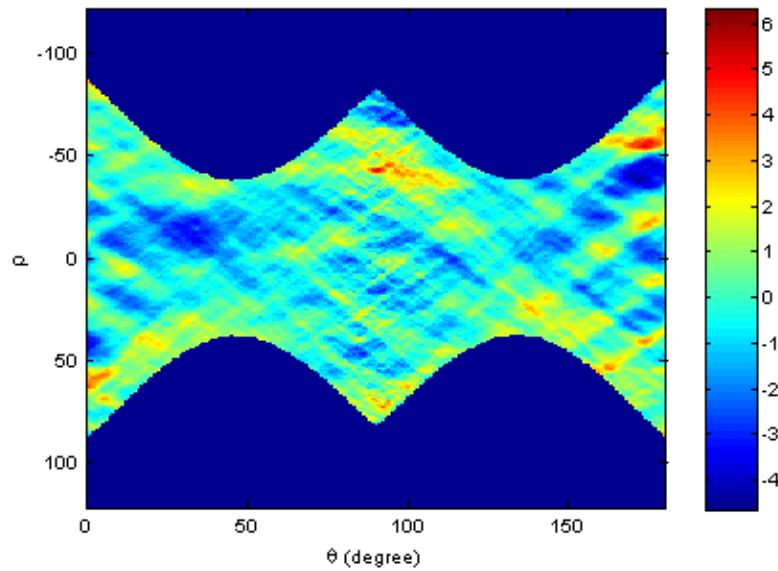


Figure 27: 2D Radon spectrum of real radar data of sea clutter.

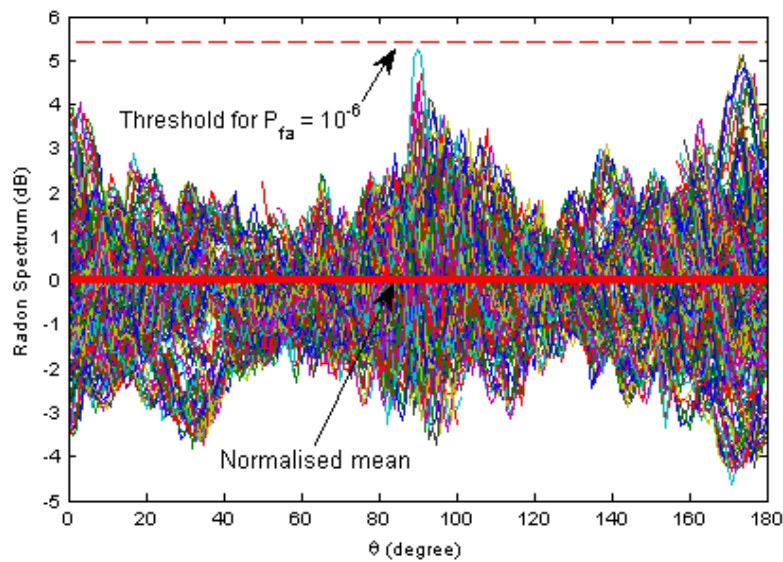


Figure 28: Radon spectrum plotted in 1D. A fixed threshold corresponding to $P_{fa} = 10^{-6}$ is also drawn assuming the data has a lognormal distribution. The red thick line is the normalised mean of sea clutter in log format.

The threshold shown in Figure 28 was determined by the largest variance. As shown in Figure 28, spectrum fluctuations against orientation angle are not uniform. In other words, correlation is directional (as is to be expected), strong in some directions and weak in others. It can be seen from Figure 28 that for this particular example, correlations in fast-time (i.e. range bin to range bin, corresponding to $\theta = 90^\circ$) as well as in slow-time (i.e. scan

to scan, corresponding to $\theta = 0, 180^\circ$) are the strongest (largest fluctuations in the spectrum), while correlations along diagonal directions are the weakest (smallest fluctuations in the spectrum).

A fixed threshold determined by the largest variance is fine, but may be too conservative (too high) for areas that have low correlations. With this in mind, the fixed threshold is replaced by an adaptive threshold. The difference is that while a fixed threshold is independent of θ and determined by using the minimum equivalent number of looks, a dynamic threshold is a function of θ , and determined by the use of the equivalent number of looks $N_{eq}(\theta)$ in that specific orientation. Accordingly, the adaptive threshold is determined by,

$$P_{faN} = P(q > q_T) = \frac{1}{2} \left(1 - \operatorname{erf} \left(\frac{q_T(\theta) - \bar{q}}{\sqrt{2\sigma_q^2 / N_{eq}(\theta)}} \right) \right) \quad (24)$$

According to (22), one has,

$$\sigma_q^2 / N_{eq}(\theta) = \operatorname{var} \{ \bar{R}_f(\theta) \} \quad \text{or} \quad N_{eq}(\theta) = \sigma_q^2 / \operatorname{var} \{ \bar{R}_f(\theta) \} \quad (25)$$

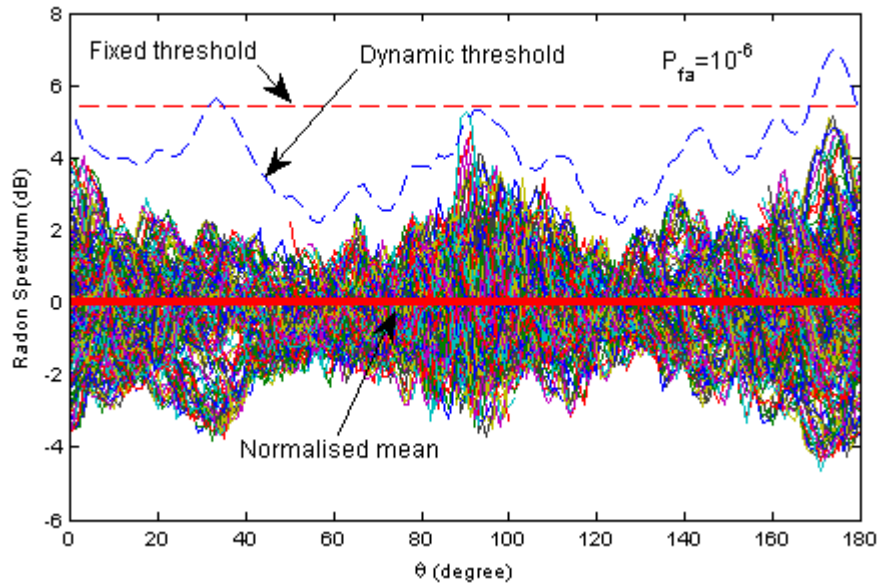


Figure 29: Radon spectrum plotted in 1D. An adaptive threshold as well as a fixed threshold corresponding to $P_{fa} = 10^{-6}$ is drawn assuming the data to be a lognormal distribution.

Therefore, the calculation of the adaptive threshold is easy. The calculated adaptive threshold for $P_{fa} = 10^{-6}$ is shown in Figure 29. Overall, the adaptive threshold is better than the fixed threshold. In some areas, the target detection requires much lower SCR values. With this adaptive threshold, there is one false-alarm at $\theta = 90^\circ$ and it corresponds to row 182 in the original range-scan image.

5.3.2 Sea Clutter with Target Dataset

The range-scan image of sea clutter containing a small moving target is shown in Figure 30. The trace of a moving target is seen in the image (the reddish line tilts to left, marked by 'TGT'). In addition, quite a few line patterns (tilt to right, marked by 'SW1' and so on) are also seen, which are believed to be sea swells.

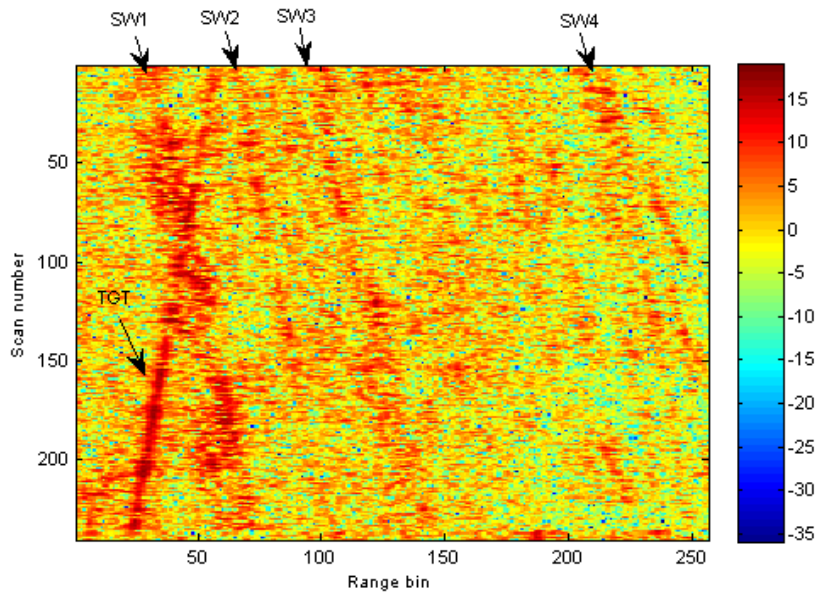


Figure 30: Image of range-scan data containing a moving target. The target trace and four dominated swells are marled.

Similar to the last dataset, the distribution of the dataset is not K- nor lognormal distributed. However, we assume that the data in the log format is normally distributed. The variance of the original single-look and the variances of multi-look in fast-time (range, i.e. the row direction) and slow-time (scan, i.e. in the column direction) are given in Table 4. It shows that the correlation in the slow-time (scan to scan) is much higher than in the fast-time (range bin to range bin).

Table 4: Original variance and variances after multi-look averaging in scan and in range for the sea clutter plus target dataset in log format.

Data	Number of looks	Variance	Equivalent number of looks
Original data	1	39.49	1
Averaging in scan	240	3.29	12.0
Averaging in range	256	0.53	74.8

Figure 31 shows the 2D Radon spectrum of the dataset. The highest value spot shown in the spectrum corresponds to the target trace. Spots in the spectrum corresponding to the marked swells are also marked in the same way in the figure. The 1D Radon spectrum is plotted in Figure 32. The threshold for a given $P_{fa} = 10^{-6}$ is also drawn in the figure, assuming that the data in the log format is normally distributed, and the equivalent number of scans to be 12.0, according to Table 4, was used in determining the threshold. The target has been robustly detected with one marginally detected false-alarm. Again we see that the fixed threshold is too conservative for some areas where the correlation is low. It should be pointed out that the calculation of correlation did not exclude the target signals which in turn would affect the calculation of threshold. However, since target signals were not dominant, the bias in the threshold should not be significant.

The 1D Radon spectrum with both the adaptive threshold and the fixed threshold for $P_{fa} = 10^{-6}$ is shown in Figure 33. Overall the adaptive threshold requires a much lower SCR value for detection. In this case the target has again been robustly detected with one marginally detected false-alarm with the adaptive threshold.

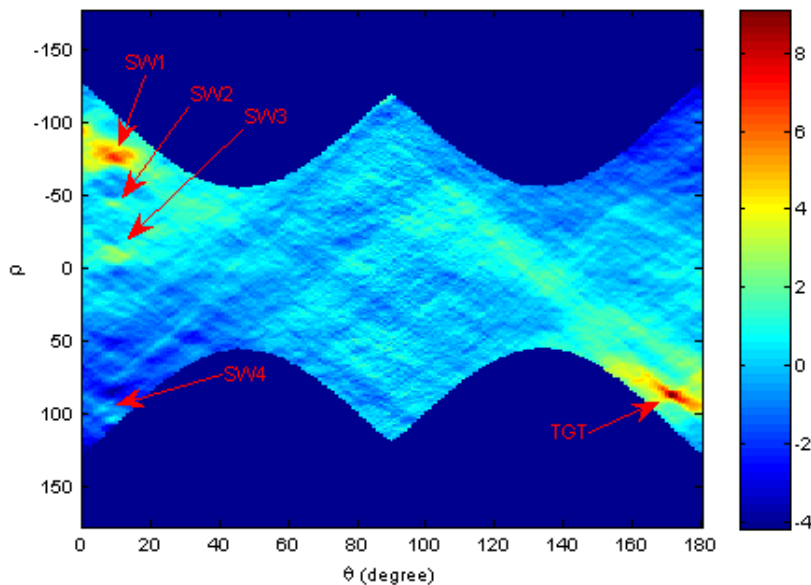


Figure 31: 2D Radon spectrum for the dataset containing a target. The target and swells result in two highest responses.

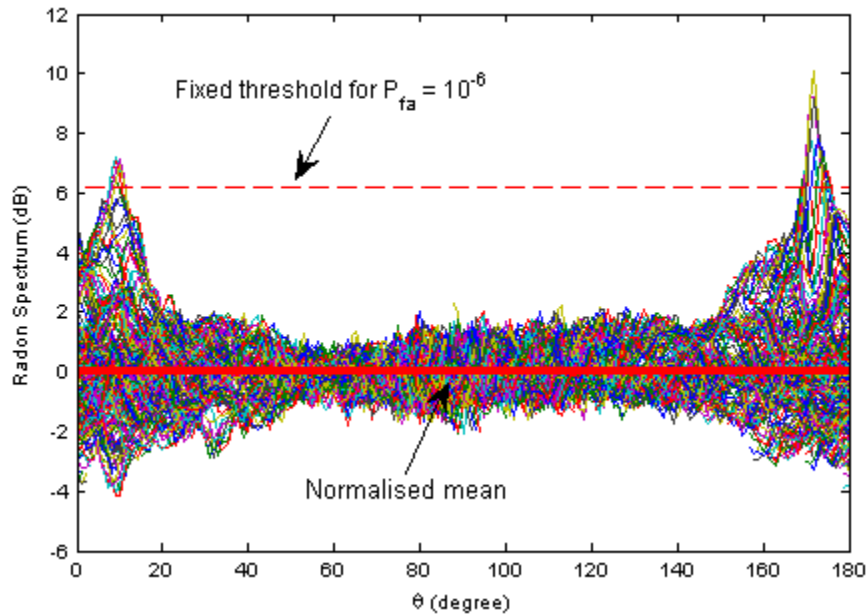


Figure 32: Radon spectrum plotted in 1D. A fixed threshold corresponding to $P_{fa} = 10^{-6}$ is also drawn assuming the data has a lognormal distribution. The target (right peak) is robustly detected together with one marginally-detected false-alarm (left peak) caused by a strong tilting line pattern of sea swells. The red thick line is the normalised mean of the sea clutter in the log format.

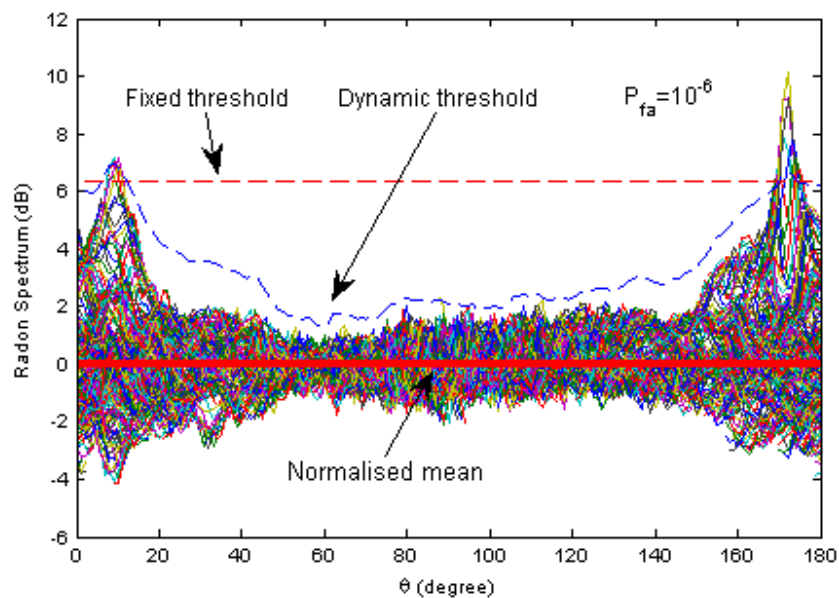


Figure 33: The adaptive threshold is much better than the fixed threshold as the former requires overall a much lower SCR value for target detection. With the adaptive threshold, the target is again robustly detected with one marginally-detected false-alarm caused by a strong line pattern possibly formed by swells.

In coherent processing, the adaptive threshold varies depending on the spectrum of the sea clutter. This is also true for non-coherent processing. Depending on radar parameters and the sea surface condition, the correlation in the range-time image generally varies from direction to direction. Hence the adaptive threshold also varies with the orientation. As shown in Figure 33, for a declaration of target detection, it only requires a SCR a little higher than 2 dB in some directions, whereas in some other directions, the requirement increases to more than 6 dB.

5.4 Case of Airborne Ingara Data

DSTO conducted a maritime radar data collection trial back in 1999. The trial used the DSTO owned airborne Ingara radar system and collected quite a few datasets over the open ocean surface approximately 10 nautical miles from the Darwin coastline (Antipov et al. 1999). One dataset (run22886) that contains some controlled moving targets is analysed here. Parameters of the radar and the ground truth for the dataset are given in Table 5.

Table 5: Radar parameters and the ground truth data.

Radar Parameter	Value
Carrier frequency	9.375 GHz (X-band)
Polarisation	VV
Chirp bandwidth	96 MHz
A/D sample rate	100 MHz
Range bin size (resolution)	1.5 m (1.56 m)
Pulse width	8 μ s
PRF	500 Hz
Antenna azimuth beamwidth	3.8°
Antenna elevation beamwidth	8°
Data collection mode	Stare
Platform height	182 m
Near range	7928 m
Flying direction	North-easterly 45° from north
Platform speed	N/A
Ground truth parameters	Value [#]
Sea state number	2-3
Swell height	3-4 m
Swell length	15 m
Swell period	10-12 sec
Swell direction	From northwest
Wind speed	10-12 knots
Wind direction	From northwest to southeast
Target Parameters	Value
Number of targets and their RCS	Two 5 m ² and two 1 m ²
Targets moving direction	North-easterly 70° from north
Targets speed	2.8-4.5 knots

[#]The ground truth data were not directly measured by any instrument; rather they were merely human observation values from a boat *in situ*.

The controlled moving targets were realised in the following way. A 27-foot recreational fishing boat was used to tow four targets consisting of two RCS of 5 m^2 and two RCS of 1 m^2 , respectively. The targets were made of bi-cone metal reflectors. The distance between the boat and the first 5 m^2 target was 100 m, followed by the second 5 m^2 target and then two smaller targets. Intervals among the four targets were 50 m apart. The recorded boat speed was between 2.8 to 4.5 knots.

Figure 34 shows a range-pulse image representing a part of run22886 dataset. The original data were further pulse down sampled by a factor of 10, (i.e. the number of pulses shown in the figure represents a PRF of 50 Hz or a scan rate of 3000 rpm). The extracted data block shown in the figure has a size of $N_x = 300$ (number of range bins) and $N_y = 400$ (number of pulse/scans). Traces of the towing boat and four towed targets are marked. The aircraft can be assumed to fly in a straight line fashion with a constant speed during the data collection and much faster than the moving targets. The towing boat also travelled approximately in a straight line fashion according to its GPS recordings (Antipov et al. 1999). Relative to the aircraft's speed the movement of targets was much slower. Because the aircraft flew in a straight line fashion with respect to the targets, the range between the two varies. If the range is the closest for the current pulse, the range was / will be longer for the earlier / later pulses. As a result, traces of the towing boat and the four towed targets show parabolic-like curves in the image. Since traces of targets are not rectilinear, we will see later that each of their energy spreads in the Random spectrum (occupying a few degrees in orientation angle θ and different lengths in radius ρ), resulting in unavoidable peak losses.

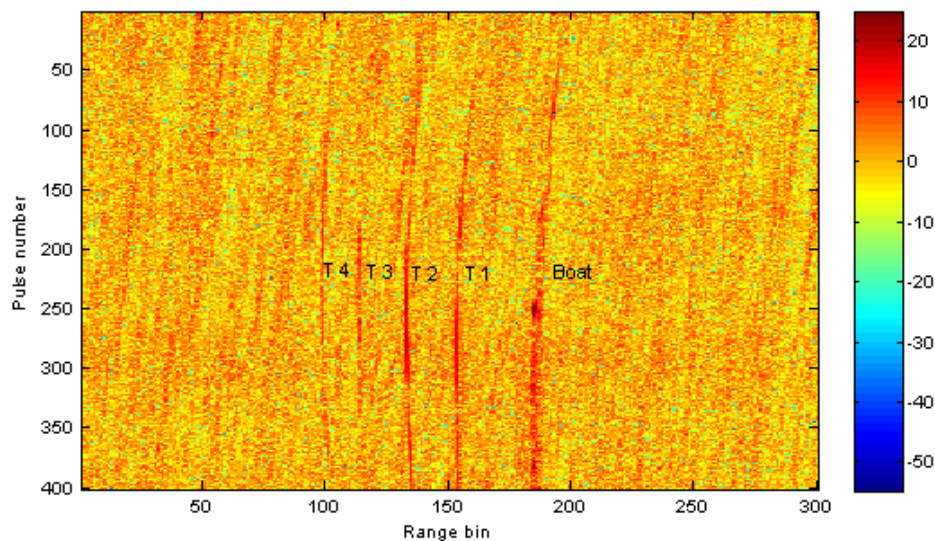


Figure 34: Range-pulse image of a part of run22886 containing the towing boat (marked by 'Boat') and four towed targets (marked by 'T1', 'T2', 'T3' and 'T4', respectively).

The empirical pdf of the data and the associated K- and lognormal fit are shown in Figure 35. While both of the two distributions do not perfectly fit the data's distribution, the K-

distribution matches better. The departure of the empirical pdf of the data from the fitted K-distribution in the upper tail region is more likely caused by the higher returns of targets, as the data distribution does not exclude the target returns.

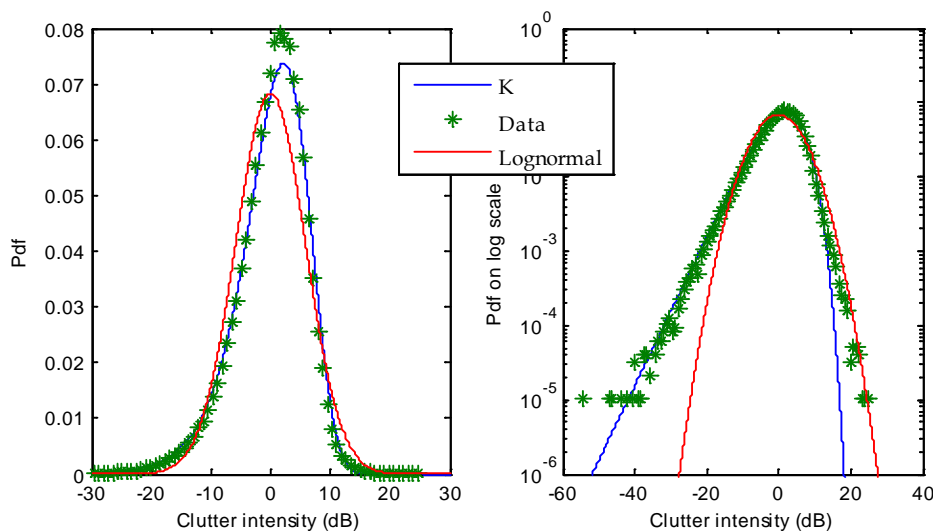


Figure 35: Empirical pdf of the data with the fit of K- and lognormal distributions.

The fitted K-distribution has a shape parameter of $\nu = 3.6$. According to the discussions in Section 3, the amplitude should be used in the detection processing. However, since the lognormal distribution provides simple calculation for the detection threshold, the data was assumed to be lognormal for simplicity. Processing using the amplitude and the decibel will then be compared later.

Figure 36 shows the 2D Radon spectrum of the range-pulse image shown in Figure 34. Locations in the spectrum for the towing boat and the towed targets are indicated. It should be pointed out that the Radon transforms at $\theta = 0^\circ$ and at $\theta = 180^\circ$ are equal but with opposite ρ values. Therefore the location of the towing boat is $\rho > 0$ at $\theta = 0^\circ$ but it is flipped to $\rho < 0$ at $\theta = 180^\circ$, and so on as indicated in Figure 36.

The conventional non-coherent integration with respect to pulse/scan is a special case of Random spectrum with $\theta = 0^\circ$. The comparison of the two is shown in Figure 37 where it can be seen that they are almost identical except for some peak losses (about 0.5 dB) for the Radon spectrum caused by the numerical implementation of the Radon transform in Matlab.

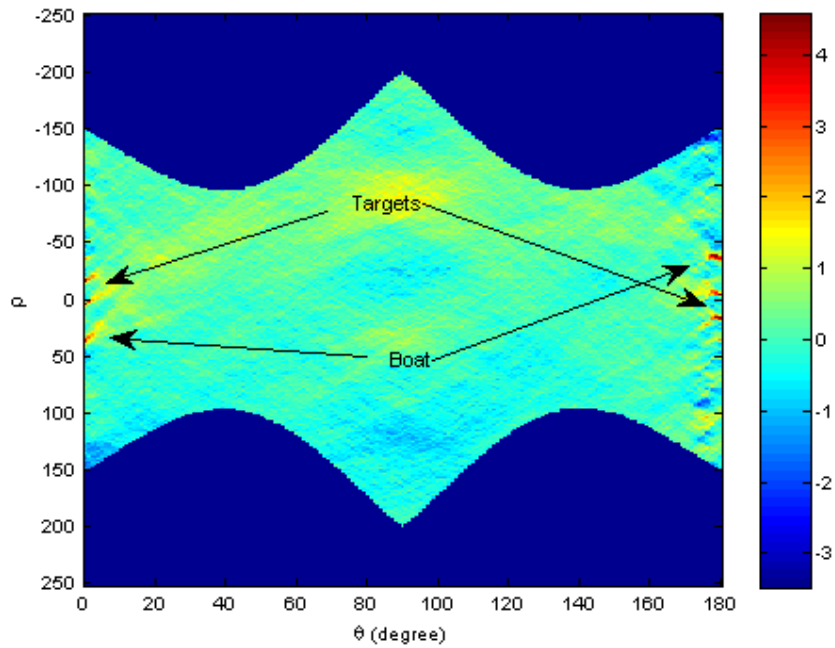


Figure 36: 2D Radon spectrum of the range-pulse image of Figure 34. Locations of the towing boat and the towed targets in the spectrum are indicated.

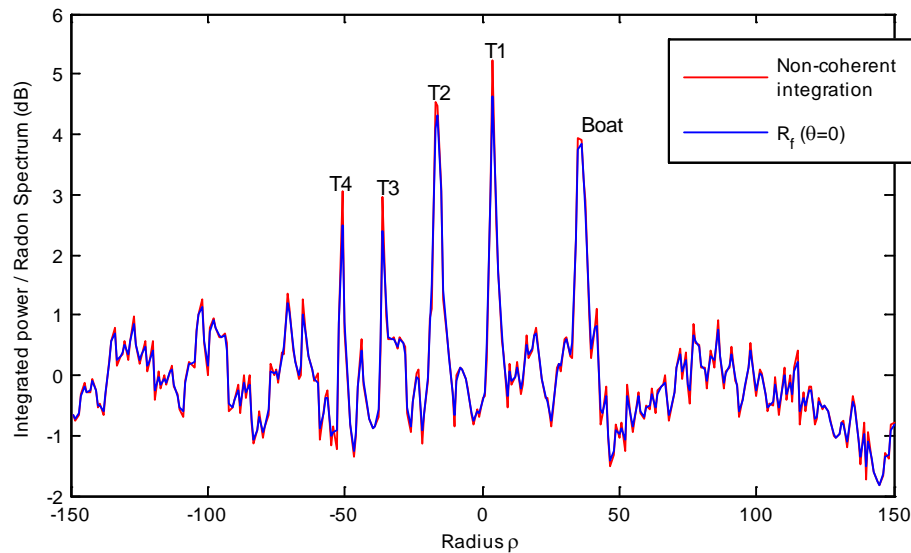


Figure 37: Conventional non-coherent integration with respect to pulse/scan is a special case of the Radon spectrum at $\theta = 0$.

In order to view details of the Radon spectrum at the vicinity of $\theta = 180^\circ$, the zoomed-in 2D Radon spectrum is shown in Figure 38 where locations of the towing boat as well as the four towed targets are indicated. Since ρ changes its sign from $\theta = 180^\circ$ to $\theta = 0^\circ$, to see

the continuity of the Radon spectra of targets, ρ has been flipped for $\theta = 1, 2, 3$ and 4 degrees in the figure. It can be seen that the energy of each target spreads over a few degrees in orientation and different radii in radius since their traces in the range-Doppler image are not in a rectilinear fashion.

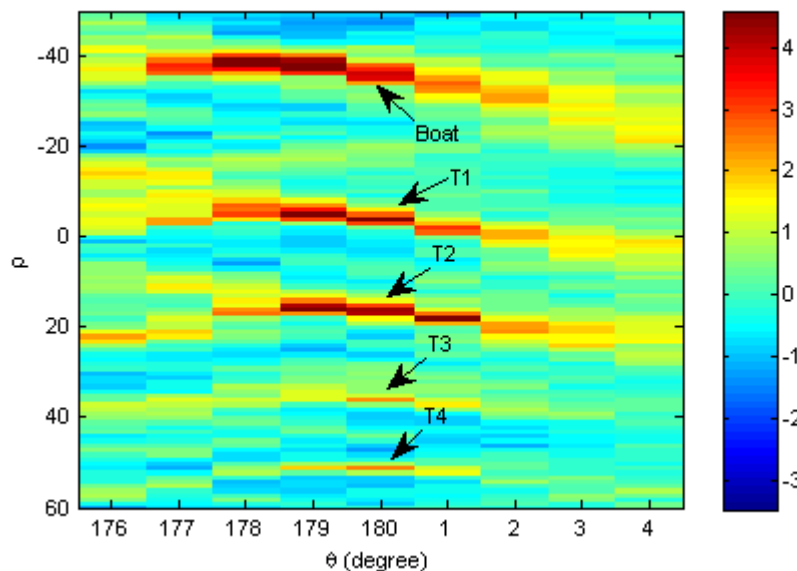


Figure 38: Zoomed-in 2D Radon spectrum showing the Radon spectra of towing boat and towed targets (note that to view the continuity of the target spectra, ρ has been flipped for $\theta = 1, 2, 3$ and 4 degrees).

The 1D Radon spectrum against orientation with the fixed detection threshold and the adaptive threshold for a false-alarm rate of $P_{fa} = 10^{-6}$ is shown in Figure 39. It can be seen that the fixed threshold is too conservative and the adaptive (dynamic) threshold would significantly improve the detection. It is also seen that the adaptive threshold raises sharply at both $\theta = 0^\circ$ and $\theta = 180^\circ$. While it is possible because of strong sea spikes in these orientations resulting in high thresholds, it is in fact due to the contamination, i.e. strong target signals are included in the calculation. If the strong target signals were excluded in the calculation, the resulting threshold would be much lower (we will see this later). However, the exclusion of target signals requires prior knowledge of targets or using more sophisticated algorithms (e.g. Cao 2006), which is out of the scope of the report.

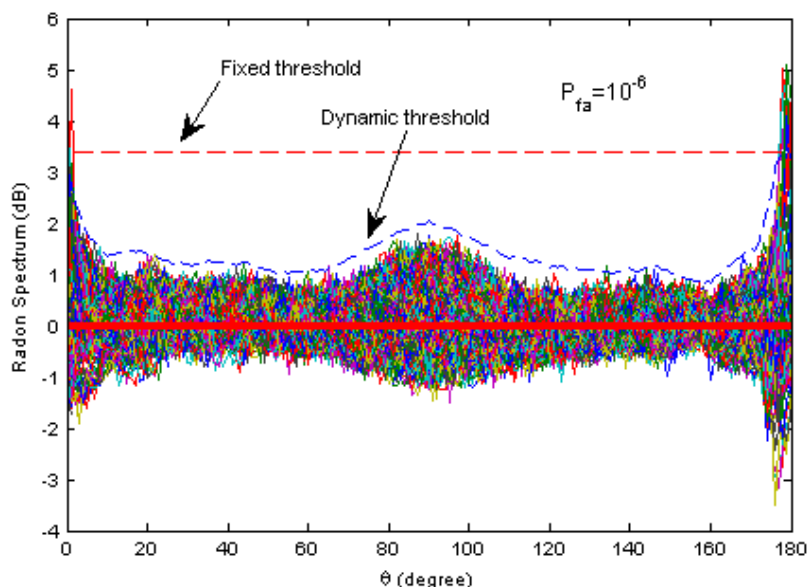


Figure 39: 1D spectrum with the fixed detection threshold and the adaptive detection threshold for $P_{fa} = 10^{-6}$, assuming the distribution of data to be lognormal.

Since target responses are all in the vicinity of $\theta = 180^\circ$ and $\theta = 0^\circ$ the 1D spectrum against radius is plotted in Figure 40 providing a better view for the responses of the targets. Since the radii of targets at $\theta = 0^\circ$ and $\theta = 180^\circ$ flip, only the region of $90^\circ \leq \theta \leq 180^\circ$ is plotted. The fixed-threshold and the adaptive threshold for $\theta = 180^\circ$ are also shown. It can be seen that while there are no false-alarms, the two smaller targets are also not detected. In fact even the adaptive threshold is also conservative, because target signals were included in the threshold calculation. After target contamination was excluded in the threshold calculation, the resulted threshold was much lower, as also shown in the figure. With this new threshold, the two smaller targets are also detected. This example demonstrates that the contamination by strong targets in calculating the statistics of clutter will raise the threshold significantly and hence mask the weak targets if they have the same orientation in the Radon transform processing.

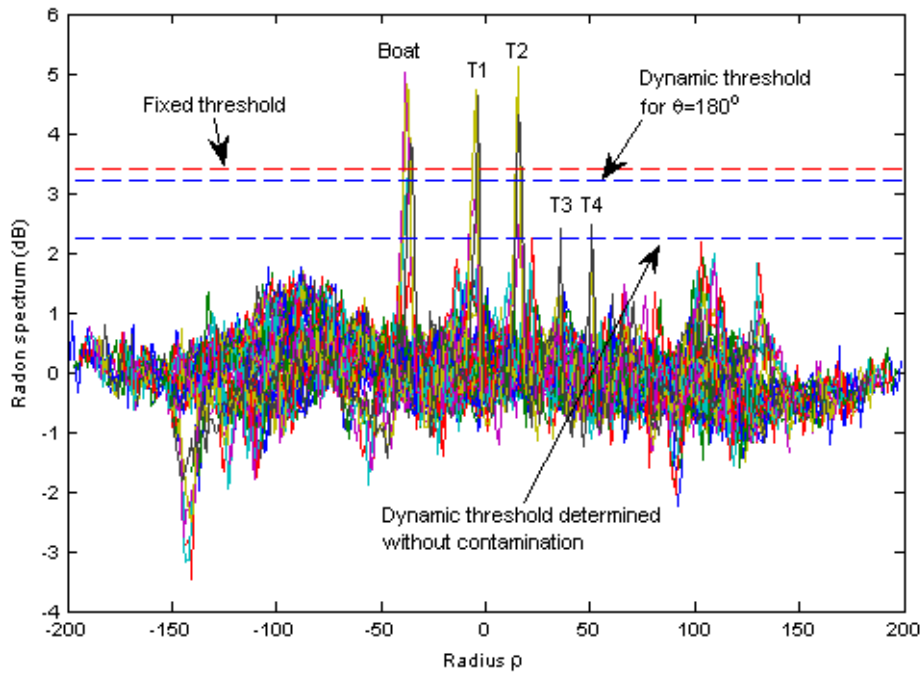


Figure 40: 1D Radon spectrum against radius ρ for $90^\circ \leq \theta \leq 180^\circ$ to show the responses of the towing boat and the four towed targets. Three different thresholds for $P_{fa} = 10^{-6}$ are also shown.

For simplicity, the above analysis assumed the dataset to be lognormally distributed. In fact we confirmed earlier that the K-distribution with $\nu = 3.6$ is a better fit for the dataset. Hence it is better to use the quantity of amplitude than decibel for non-coherent integration detection (i.e. for the Radon transform). To confirm, the 1D Radon spectra obtained from using the quantities of amplitude and decibel are plotted in Figure 41 for comparison. In order to make a fair comparison the Radon spectrum of amplitude was further normalised and the same scale was used in plotting. It can be seen that while the rest of the spectra are very much alike one the other, the responses of strong targets are about 0.5 to 1.0 dB higher in the spectrum of amplitude. The drawback of using the amplitude is that the threshold for a given false-alarm rate cannot be easily determined, especially when clutter is correlated.

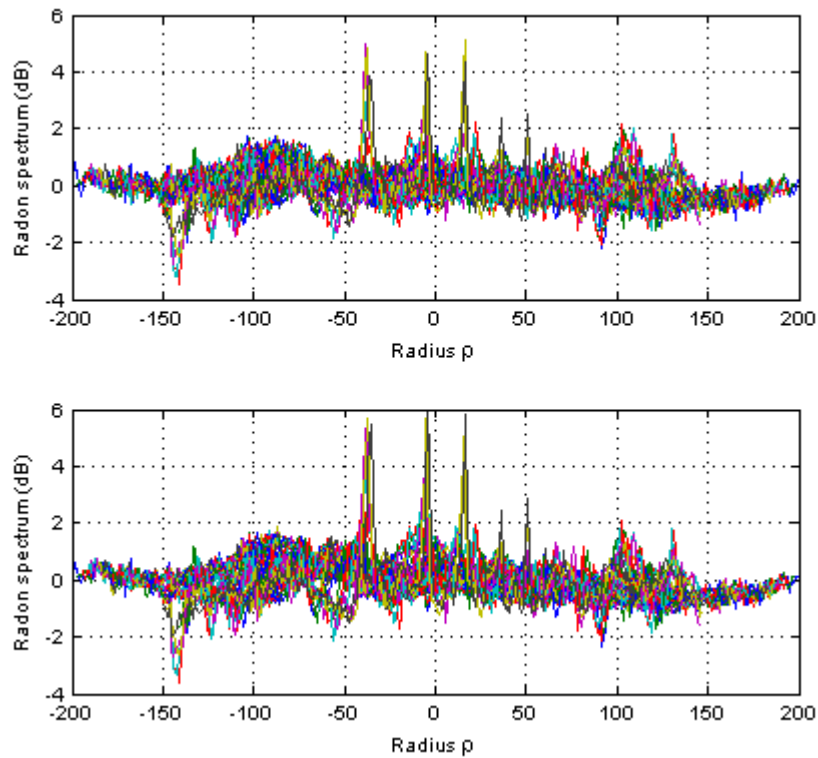


Figure 41: Comparison of Radon spectra obtained by the use of (top) decibel and (bottom) amplitude. Note that the spectrum of amplitude is then normalised for ease of comparison ($90^\circ \leq \theta \leq 180^\circ$).

If the trajectory of a moving target is rectilinear, its energy spreads in the Radon spectrum as shown in Figure 38. It means that an increase in the original image size does not necessarily improve the detection, because only a partial line of the whole integration line corresponding to a particular pair of (θ, ρ) contains the target signal that reduces the overall average SCR or SNR. This may also be considered as the signal integral loss with respect to the non-rectilinear condition. For non-linear motion (no matter what are the causes) targets, using shorter integral lengths (i.e. using a smaller image to calculate the Radon spectrum) may lead to better results. The Radon spectrum of a subset of Figure 34 consisting of 200 pulses (from pulse 151 to pulse 350) and 400 range bins (i.e. the number of range bins remains the same) were computed and the 1D Radon spectrum against ρ for $90^\circ \leq \theta \leq 180^\circ$ is shown in Figure 42. In comparison with Figure 40, it can be seen that SCRs for all five targets were improved though only a half of the original pulses were used in the processing.

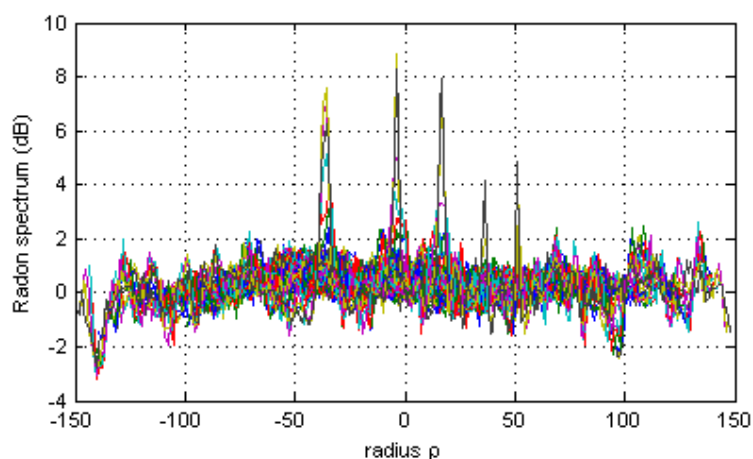


Figure 42: 1D Radon spectrum against radius ρ for $90^\circ \leq \theta \leq 180^\circ$ to show the responses of the towing boat and the four towed targets. The spectrum was produced using a reduced image size of 200 scans by 400 range bins from the original image size of 400 scans by 400 range bins shown in Figure 34.

This example shows that it is essential to constrain the trajectory of moving target in the 2D image in a straight line fashion when the Radon spectrum is used in detection processing. Normally for a short duration, most of radar targets of interest can be assumed to have a constant velocity, so is the radar platform. However, although both the radar and the target travel in a straight line fashion, the trace of the target in the range-time image may not be rectilinear. The key is the range reference the radar uses to form the data. Since the Radon transform performs best for detecting straight line patterns, it is desirable for radar to use a proper range compensation scheme, so that the range of the point of interest stays unchanged. As a consequence, a stationary target resides in the same range bin, and a linearly moving target leaves a linear trace in the range-time real-aperture radar image, or in the range-cross-range synthetic-aperture radar image. Figure 43 depicts the range reference the radar is supposed to use so that the point of interest maintains a constant range. This range reference system is in fact also used in the spotlight-mode SAR image formation. The difference is that in the spotlight-mode SAR processing is coherent, so focus is critical and the range has to be within an accuracy of a fraction of the wavelength (in centimetres). For the non-coherent integration processing, however, range accuracy within a fraction of the range resolution (in metres) would be sufficient.

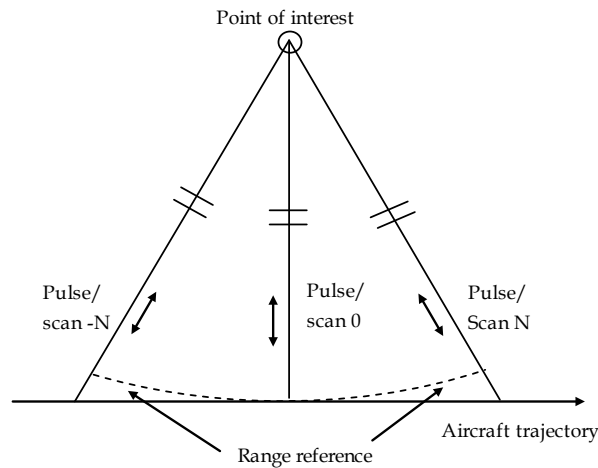


Figure 43: Range reference for a moving radar, so that the point of interest has a constant range. This reference is also used in the spotlight-mode SAR data processing.

6. Conclusions

We have introduced the concept of the Radon spectrum which is just a kind of normalised Radon transform. It is applied to non-coherent processing for small target detection. The detection threshold and probability of detection for a given false-alarm rate discussed in conventional non-coherent detection for a stationary target can simply be brought forward to the Radon spectrum. Visually, the 2D Radon spectrum of a range-scan (range-time) 2D radar image in non-coherent processing is analogous to the 2D range-Doppler spectrum of a 2D range-pulse (range-time) radar image in coherent processing. The algorithm is applicable to any kind of two dimensional dataset, such as range-time real-aperture radar data, range-cross-range synthetic aperture radar data, as long as the target trace in the image appears to be rectilinear.

Whether there is range migration of the moving target is not a concern and does not make any difference to detection using the Radon spectrum, provided the movement of the target is rectilinear. A stationary target is only a special case of zero velocity and the results given by the Radon spectrum shall be identical to the traditional non-coherent integration. Whether exposure of the target is continuous is also not a concern, as long as its trace is rectilinear and the trace is captured by the radar.

An adaptive threshold is proposed to deal with correlated sea clutter. The correlation of sea clutter is directional in the 2D range-time domain. The correlation results in a smaller equivalent number than the actual number of multi-looks in the processing, and the corresponding threshold also needs to be raised accordingly. The adaptive threshold adaptively varies to meet the requirement of CFAR.

Depending on the nature of the data, quantities one should use in the processing have been discussed. For K-distributed data, if its slowly-varying component also varies in the slow-time domain (scan-to-scan, for instance), different quantities should be used in the processing depending on the shape parameter. As a general rule of thumb, we suggest use of the following quantities for scan-to-scan non-coherent integration processing,

- Log data if $\nu \leq 1.0$
- Amplitude if $1 < \nu < 10$
- Intensity if $\nu > 10$

However, for the real radar data tested in this report, we have found the lognormal distribution is also a good fit to some sea clutter.

Both simulated and real radar datasets have been tested and have demonstrated the effectiveness of the proposed detection mode. A target with a few dB SCR can be detected robustly. After detection in the Radon spectrum, positions of the target in its original range-time image, its radial velocity and RCS can be determined accordingly.

To reduce the computational cost, the question of how to implement the Radon transform in a fast way may be a topic for the future research. This is particularly important because in an operational surveillance radar system with a scanning antenna, the Radom transform would need to be computed for each and every azimuth beam position.

7. Acknowledgement

Feedback, comments and grammar corrections from Drs P. Berry and B. Haywood are greatly acknowledged. The author also thanks Dr A. P. Shaw for his explanation of the data collection and processing of the Kelvin Hughes 'SharpEye' radar, as well as his technical comments.

8. References

- Allen, M. R., Katz, S. L., and Urkowitz, H. (1989), "Geometric aspects of long-term noncoherent integration", *IEEE Trans on Aerospace and Electronic Systems*, **25**(5), 689-700.
- Antipov, I., McCarthy, J., and Baldwinson, J. (1999), "Maritime radar data collection trial ESRL 38/97", DSTO-TP-98/084, Defence Science and Technology Organisation, Australia.
- Armstrong, B. C., and Griffiths, H. D. (1991), "CFAR detection of fluctuating targets in spatially correlated K-distributed clutter", *Radar and Signal Processing, IEE Proceedings F*, **138**(2), 139-152.
- Ballard, D. H. (1981), "Generalising the Hough transform to detect arbitrary shapes", *Pattern Recognition*, **13**(2), 111-122.
- Bracewell, R. N. (1995), *Two-Dimensional Imaging*, Englewood Cliffs, NJ, Prentice Hall.
- Cao, T.-T. V. (2006), "Effects of multiple targets on the mean level STAP detector", *Proceedings of the 2006 Radar Conference*, Shanghai, China.
- Carlson, B. D., Evans, E. D., and Wilson, S. L. (1994a), "Search radar detection and track with the Hough transform -- Part I: System Concept", *IEEE Trans on Aerospace and Electronic Systems*, **30**(1), 102-108.
- Carlson, B. D., Evans, E. D., and Wilson, S. L. (1994b), "Search radar detection and track with the Hough transform -- Part II: Detection Statistics", *IEEE Trans on Aerospace and Electronic Systems*, **30**(1), 116-125.
- Carlson, B. D., Evans, E. D., and Wilson, S. L. (1994c), "Search radar detection and track with the Hough transform -- Part III: Detection performance with binary integration", *IEEE Trans on Aerospace and Electronic Systems*, **30**(1), 116-125.
- Crisp, D. J., Stacy, N. J. S., and Goh, A. S. (2006), "Ingara medium-high incidence angle polarimetric sea clutter measurements and analysis", Technical Report, DSTO-TR-1818, Defence Science and Technology Organisation, Australia.
- Dong, Y. (2012a), "Optimal coherent radar detection in a K-distributed clutter environment", *IET Radar, Sonar and Navig.*, **6**(5), 283-292.
- Dong, Y. (2012b), "Optimal detection in the K-distributed clutter environment -- non-coherent radar processing ", Technocal Report, DSTO-TR-2785, Defence Science and Technology Organisation, Australia.

- Furukawa, Y., and Shinagawa, Y. (2003), "Accurate and robust line extraction by analysing distribution around peaks in Hough space", *Computer Vision and Image Understanding*, **92**, 1-25.
- Jones, R., Cook, T., and Redding, N. J. (2004), "Implementation of the Radon transform using non-equispaced discrete Fourier transforms", Technical Report, DSTO-TR-1576, Defence Science and Technology Organisation, Australia.
- Kay, S. M. (1998), *Fundamentals of Statistical Signal Processing. Vol. II, Detection Theory*, New Jersey, Prentice Hall.
- Perry, R. P., Dipietro, R. C., and Fante, R., L. (1999), "SAR imaging of moving targets", *IEEE Trans on Aerospace and Electronic Systems*, **35**(1), 188-200.
- Perry, R. P., Dipietro, R. C., and Fante, R., L. (2007), "Coherent integration with range migration using keystone formatting", *Proceedings of IEEE Radar Conference*.
- Rosenberg, L. (2012), "Sea-spike detection in high grazing angle X-band sea-clutter", DSTO-TR-2820, Defence Science and Technology Organisation, Australia.
- Shaw, A. P. (2013), "Christmas Island radar system detection processing (version 6.6) (For Official Use Only)", DSTO-TR-2841, Defence Science and Technology Organisation, Australia.
- Ward, K. D., Tough, R. J. A., and Watts, S. (2006), *Sea Clutter: Scattering, the K Distribution and Radar Performance*, London, Institute of Engineering Technology.
- Watts, S. (1987), "Radar detection prediction in K-distributed sea clutter and thermal noise", *IEEE Trans. on Aerospace and Electronic Systems*, **AES-23**(1), 40-45.
- Wilks, S. S. (1962), *Mathematical Statistics*, New York, John Wiley & Sons.
- Xu, J., Yu, J., Peng, Y.-N., and Xia, X.-G. (2011), "Radon-Fourier transform for radar target detection, I: generalised Doppler filter bank", *IEEE Trans on Aerospace and Electronic Systems*, **47**(2), 1186-1202.
- Yu, J., Xu, J., Peng, Y.-N., and Xia, X.-G. (2012), "Radon-Fourier transform for radar target detection (III): Optimality and fast implementations", *IEEE Trans on Aerospace and Electronic Systems*, **48**(2), 991-1004.

DEFENCE SCIENCE AND TECHNOLOGY ORGANISATION DOCUMENT CONTROL DATA						
					1. DLM/CAVEAT (OF DOCUMENT)	
2. TITLE Radon Spectrum and Its Application for Small Moving Target Detection				3. SECURITY CLASSIFICATION (FOR UNCLASSIFIED REPORTS THAT ARE LIMITED RELEASE USE (L) NEXT TO DOCUMENT CLASSIFICATION) Document (U) Title (U) Abstract (U)		
4. AUTHOR(S) Yunhan Dong				5. CORPORATE AUTHOR DSTO Defence Science and Technology Organisation PO Box 1500 Edinburgh South Australia 5111 Australia		
6a. DSTO NUMBER DSTO-TR-3103		6b. AR NUMBER AR-016-290		6c. TYPE OF REPORT Technical Report		7. DOCUMENT DATE April 2015
8. FILE NUMBER	9. TASK NUMBER	10. TASK SPONSOR		11. NO. OF PAGES 50		12. NO. OF REFERENCES 24
13. DSTO Publications Repository http://dspace.dsto.defence.gov.au/dspace/				14. RELEASE AUTHORITY Chief, National Security and ISR Division		
15. SECONDARY RELEASE STATEMENT OF THIS DOCUMENT <i>Approved for public release</i>						
OVERSEAS ENQUIRIES OUTSIDE STATED LIMITATIONS SHOULD BE REFERRED THROUGH DOCUMENT EXCHANGE, PO BOX 1500, EDINBURGH, SA 5111						
16. DELIBERATE ANNOUNCEMENT No Limitations						
17. CITATION IN OTHER DOCUMENTS Yes						
18. DSTO RESEARCH LIBRARY THESAURUS Maritime radar Non-coherent detection Radon transform Radon Spectrum						
19. ABSTRACT Analogous to the radar Doppler spectrum for coherent processing, the concept of a Radon spectrum that is a kind of normalised Radon transform is proposed and used for radar non-coherent detection. One advantage of using the Radon transform for non-coherent processing is that integration in all directions is considered, and hence range migration of moving targets is not a concern. The detection processing is based upon a 2D Radon spectrum that is transformed from the original range-time 2D radar image. The threshold and the probability of detection for a given false-alarm rate are determined in the same way as the traditional non-coherent integration. Both simulated and real radar datasets are tested and the effectiveness of the proposed technique is demonstrated.						